The role of iron and myelin in orientation dependent R_2^* of white matter

Journal:	*NMR in Biomedicine*
Manuscript ID	NBM-18-0195.R2
Wiley - Manuscript type:	Research Article
Date Submitted by the Author:	n/a
Complete List of Authors:	Kor, Daniel; University of British Columbia, Physics and Astronomy ; University of British Columbia, UBC MRI Research Centre Birkl, Christoph; University of British Columbia, UBC MRI Research Centre; University of British Columbia, Department of Pediatrics (Division of Neurology); Medical University of Graz, Department of Neurology Ropele, Stefan; Medical University of Graz, Department of Neurology Doucette, Jonathan; University of British Columbia, Physics and Astronomy ; University of British Columbia, UBC MRI Research Centre; University of British Columbia, Department of Pediatrics (Division of Neurology) Xu, Tianyou; University of Oxford, Oxford Centre for Functional MRI of the Brain Wiggermann, Vanessa; University of British Columbia, Hernández-Torres, Enedino; University of British Columbia, UBC MRI Research Centre; University of British Columbia, Department of Pediatrics (Division of Neurology) Hametner, Simon ; University Medical Center Goettingen, Institute of Neuropathology Rauscher, Alexander; University of British Columbia, UBC MRI Research Centre; University of British Columbia, Department of Pediatrics (Division of Neurology)
Keywords:	Susceptibility weighted imaging < Endogenous Contrast Methods < Methods and Engineering, Relaxometry < Endogenous Contrast Methods < Methods and Engineering, Neurodegenerative diseases < Neurological < Applications, White matter diseases < Neurological < Applications

The role of iron and myelin in orientation dependent R_2^* of white matter

Daniel Kor[1,2], Christoph Birkl[2,3,4], Stefan Ropele[4], Jonathan Doucette[1,2,3], Tianyou Xu[5], Vanessa Wiggermann[1,2,3], Enedino Hernández-Torres[2,3], Simon Hametner[6], Alexander Rauscher[1,2,3,7]

[1] Department of Physics & Astronomy, University of British Columbia, Vancouver, BC, Canada
[2] UBC MRI Research Centre, University of British Columbia, Vancouver, BC, Canada
[3] Department of Pediatrics (Division of Neurology), University of British Columbia, Vancouver, BC, Canada
[4] Department of Neurology, Medical University of Graz, Graz, Austria
[5] Oxford Centre for Functional MRI of the Brain, University of Oxford, Oxford, United Kingdom
[6] Institute of Neuropathology, University Medical Center Göttingen, Göttingen, Germany
[7]Department of Radiology, University of British Columbia, Vancouver, BC, Canada

Corresponding Author
Daniel Kor
Department of Physics and Astronomy
UBC MRI Research Centre

University of British Columbia
M10 - Purdy Pavilion
2221 Wesbrook Mall
Vancouver, BC V6T 2B5
E-mail: daniel.kor@alumni.ubc.ca
Tel: +1 604 827 5462
Fax: +1 604 827 3339

Word count: 5,543

Keywords: MRI; R_2^*; white matter fibre orientation; brain iron; myelin; multiple sclerosis; neurodegenerative disease; susceptibility-weighted imaging

Short title: Iron and myelin in orientation dependent R_2^*

Abbreviation used: WM, white matter; MVF, myelin volume fraction; MC, myelin content characterized by myelin water fraction; MWF, myelin water fraction; IC, iron concentration

Abstract

Brain myelin and iron content are important parameters in neurodegenerative diseases such as multiple sclerosis (MS). Both myelin and iron content influence the brain's R_2^* relaxation rate. However, their quantification based on R_2^* maps requires a realistic tissue model that can be fitted to the measured data. In structures with low myelin content, such as deep gray matter, R_2^* shows a linear increase with increasing iron content. In white matter, R_2^* is not only affected by iron and myelin but also by the orientation of the myelinated axons with respect to the external magnetic field. Here, we propose a numerical model which incorporates iron and myelin, as well as fibre orientation, to simulate R_2^* decay in white matter. Applying our model to fibre orientation-dependent *in vivo* R_2^* data, we are able to determine a unique solution of myelin and iron content in global white matter. We determine an averaged myelin volume fraction of 16.02 ± 2.07% in non-lesional white matter of patients with MS, 17.32 ± 2.20% in matched healthy controls, and 18.19 ± 2.98% in healthy siblings of patients with MS. Averaged iron content was 35.6 ± 8.9 mg/kg tissue in patients, 43.1 ± 8.3 mg/kg in controls, and 47.8 ± 8.2 mg/kg in siblings. All differences in iron content between groups were significant, while the difference in myelin content between MS patients and the siblings of MS patients was significant. In conclusion, we demonstrate that a model that combines myelin-induced orientation-dependent and iron-induced orientation-independent components is able to fit *in vivo* R_2^* data.

Introduction

In the human brain, diamagnetic myelin and paramagnetic iron are major contributors to the magnetic resonance signal's R_2^* relaxation rate. In deep gray matter (DGM), post mortem studies have shown that R_2^* correlates well with tissue iron concentrations[1–3]. Therefore, R_2^* is widely used as an *in vivo* imaging measure for DGM iron[4–7]. In the white matter (WM), the situation is more complicated. Measured R_2^* relaxation in WM depends not only on the tissue composition but also on the angle θ between WM fibre tracts and the main magnetic field B_0[8–13]. This orientation dependency has been attributed to the magnetic field inhomogeneities generated by the structural anisotropy of WM tracts and the anisotropic magnetic susceptibility of myelin itself[11,13,14]. While DGM structures have the highest iron concentrations of up to 240 mg iron per kg tissue, WM contains about 30 to 45 mg iron per kg of tissue[15,16].

The radiological hallmarks of multiple sclerosis (MS) are hyperintense WM lesions on T_2-weighted MRI. In addition to focal demyelinated WM lesions, diffuse alteration of the non-lesional WM has been observed when using various MR methodologies, such as proton MR spectroscopy[17], magnetization transfer ratio[18], myelin water imaging[19], or R_2^* in combination with diffusion tensor imaging (DTI). By associating a measured R_2^* with a fibre orientation, θ, computed from DTI, the orientation dependent $R_2^*(\theta)$ can be calculated[20]. Histopathological studies have revealed diffuse and extensive damage in the normal appearing white matter (NAWM), encompassing myelin loss, axonal injury, microglia activation, and perivascular inflammatory infiltrates[21,22]. In MS, NAWM iron was found to be gradually reduced over the course of the disease[23], possibly accompanying the loss of myelin[21]. These pathological findings offer an explanation on why $R_2^*(\theta)$ differs significantly between patients with MS, healthy controls, and healthy siblings of patients with MS[20]. Therefore, there is clinical interest in quantifying both myelin and iron in the entire WM from MRI data. However, myelin and iron both increase R_2^*. An approach to separate the contribution of iron and myelin to R_2^* is to measure temperature-dependent R_2^*, which is however restricted to post mortem studies[24]. While quantitative susceptibility mapping[25] is able to distinguish paramagnetic (e.g. iron) from diamagnetic (e.g. myelin) susceptibility sources, it does not distinguish myelin loss from iron increase, as both lead to an increase in magnetic susceptibility[26].

The behaviour of the magnetic susceptibility of myelin is described by a tensor[14]. Consequently, myelin induces a modification on the local magnetic field that depends on the angle between the myelinated axon and the main magnetic field, B_0[14,27]. Since iron is predominantly stored in ferritin, a protein shell with an approximately spherical biomineral core, its modifications on the local magnetic field are orientation-independent[11]. This key difference between myelin sheaths and iron cores opens another avenue for the interrogation of tissue myelin and iron with MRI via the orientation dependency of R_2^*. Such an approach requires a model describing how R_2^* depends on these two quantities and the axons' orientation relative to B_0.

Here, we present a numerical tissue model that considers contributions from orientation-dependent myelin and orientation-independent iron. With this model, we compute orientation-dependent R_2^* from first principles. By fitting the modelled $R_2^*(\theta)$ curves to experimental data, we obtain global averages for iron and myelin contents in non-lesional WM of patients with MS, healthy siblings of patients, and unrelated healthy controls. The findings obtained from the numerical tissue model are then put into context with a previous R_2^* model[11]. Finally, by acquiring data in an orientation-independent phantom at varying combinations of diamagnetic bovine serum albumin (BSA) and paramagnetic ferritin concentrations, we explore how these two substances influence R_2^*, albeit in an orientation-independent manner.

Theory

Numerical Tissue Model

Myelinated axons and ferritin were modelled as cylinders and spheres, respectively. Axon sizes were modelled as a gamma distribution around a mean radius of 0.46 µm, with the distribution's shape parameter of 3.82, and assigned a packing density of approximately 64%[13]. For a 3T external magnetic field, a T_2 relaxation time of 15 ms was assumed for myelin water, and 63 ms for intracellular and extracellular water[28]. Each ferritin molecule was allocated a radius of 4 nm, with the sphere assumed to be filled with 4500 ferric ions[29]. Subvoxels containing ferritin were assigned a T_2 relaxation time of 0.001 ms, which is arbitrary but effectively leads to zero transverse magnetization. Myelin g-ratio and the iron concentration were left as free-varying parameters. For the simulation, the myelin sheath, which is related to myelin g-ratio, was assumed to consist of 50% water[30]. Due to the presence of ferritin, there is no cylindrical symmetry and the tissue had to be modelled in three dimensions. The ferritin molecules were randomly distributed throughout a plane centred at the simulated volume, to ensure that the magnetic field inhomogeneities generated by the ferritin were captured by the simulation volume. The intra-axonal and extra-axonal spaces were assigned a reference magnetic susceptibility of $\chi = 0$, with all other magnetic susceptibilities relative to this reference value. The magnetic susceptibility of the ferritin was assumed to be a scalar with $\chi_f = 520$ ppm[26,31]. In tensor notation, this is represented as a diagonal matrix with identical entries:

$$\chi_{ferritin} = \begin{bmatrix} \chi_f & 0 & 0 \\ 0 & \chi_f & 0 \\ 0 & 0 & \chi_f \end{bmatrix}. \tag{1}$$

The magnetic susceptibility of myelin is a rank 2 tensor:

$$\chi_{myelin} = \begin{bmatrix} \chi_i + \chi_a & 0 & 0 \\ 0 & \chi_i - \frac{\chi_a}{2} & 0 \\ 0 & 0 & \chi_i - \frac{\chi_a}{2} \end{bmatrix}, \tag{2}$$

where isotropic magnetic susceptibility of myelin is χ_i = -60 ppb and its anisotropic magnetic susceptibility is χ_a = -120 ppb[14]. To produce a simulated three-dimensional magnetic susceptibility map χ of a WM tissue voxel, the tissue compartments were assigned the magnetic susceptibilities of myelin, ferritin, as well as intra- and extra-axonal water. Prior to magnetic field computation, a coordinate transformation was performed on χ to obtain the magnetic susceptibility map in the common reference frame of the axon, χ_R:

$$\chi_R(r, \phi) = R(\phi) \cdot \chi \cdot R(\phi)^T, \tag{3}$$

where the magnetic susceptibility values are now dependent on their spatial position, defined by radial coordinate r and azimuthal coordinate ϕ, relative to the axon and R is the rotation matrix defined as:

$$R(\phi) = \begin{bmatrix} cos(\phi) & sin(\phi) & 0 \\ -sin(\phi) & cos(\phi) & 0 \\ 0 & 0 & 1 \end{bmatrix}, \tag{4}$$

The magnetic field created by this configuration was then forward calculated in the Fourier domain via Equation 5, as derived in[27]:

$$\Delta f(r,\phi) = FT^{-1}\left\{\frac{1}{3}\hat{\mathrm{H}}^{\mathrm{T}} FT\left\{\chi_R(r,\phi)\right\}\hat{\mathrm{H}} - \hat{\mathrm{H}}^{\mathrm{T}}\mathrm{k}\frac{\mathrm{k}^{\mathrm{T}} FT\left\{\chi_R(r,\phi)\right\}\hat{\mathrm{H}}}{\mathrm{k}^2}\right\}\gamma\mathrm{H}, \tag{5}$$

where $\Delta f(r,\phi)$ is the off resonance frequency in Hz, $\chi_R(r,\phi)$ denotes the spatial susceptibility tensor matrix defined relative to the reference frame of the axon, γ is the gyromagnetic ratio, FT is the Fourier Transform and FT^{-1} is the inverse Fourier Transform. The vectors $\hat{H} = [\sin(\theta), 0, \cos(\theta)]$ and $k = [kx, ky, kz]$ represent the unit direction vector of the external magnetic field and the spatial frequency vector, respectively, where θ represents the fibre orientation relative to the external magnetic field. In the simulation, the external magnetic field, H, is assumed to be 3T. For isotropic magnetic susceptibility, the tensor becomes a diagonal matrix and the forward calculation becomes a convolution with a unit dipole kernel. An illustration of the magnetic field inhomogeneities generated by the model's geometry is shown in Figure 1.

Model

The geometry of the model for both ferritin and axons spans length scales across three orders of magnitude. The myelinated axons and ferritin were simulated on a 600 × 600 × 60 array of subvoxels that corresponds to a $2.4 \times 2.4 \times 0.24\ \mu m^3$ volume. A spatial resolution of 4 nm per subvoxel was used, following the observation of numerical rounding artifacts when simulating at the initially decided spatial resolution of 8 nm.

For any given fibre orientation between 0 and 90 degrees (in 5-degree intervals), the transverse magnetization within the 3D volume was simulated for a multi-gradient echo signal up to 100 ms in steps of 5 ms. For a given echo time, the signal was computed by taking the magnitude of the integral over the complex signals in the 600 × 600 × 60 subvoxels. Note that the phase evolution during these 5 ms intervals may be more than 2π, but when computing the signal, we are only interested in the subvoxels' phase at a certain time and not how many 2π revolutions have happened until then. A single exponential was then fitted to the computed signal decay in order to simulate R_2^*.

In vivo Human Data

The numerical myelin-ferritin model described in Section *Model* was applied to $R_2^*(\theta)$ of 39 subjects with MS, 31 healthy siblings of subjects with MS, and 30 healthy unrelated controls (see Table 1 for demographic details) published previously[20]. All subjects gave their written informed consent according to the Declaration of Helsinki. All subjects were scanned on a 3T system (Philips Achieva) using an 8-channel SENSE head coil. Data for R_2^* maps were acquired with a three dimensional gradient echo sequence with five echoes (TR = 28 ms, TE_1 = 5 ms, echo spacing = 5 ms, acquired voxel size = 0.9 × 1.0 × 1.6 mm^3, reconstructed voxel = 0.8 × 0.8 × 0.8 mm^3). R_2^* maps were calculated by fitting a mono-exponential function to the signal decay in each voxel. Diffusion tensor imaging (DTI) data were collected with a spin echo planar sequence (b0 = 0, b1 = 1000, 16 directions, TR/TE = 7465/75 ms, FOV = 212 × 212 mm^2, 60 slices of 2.2 mm thickness, in-plane resolution = 2.2 × 2.2 mm^2). DTI data were analyzed using FSL[32] and fibre orientation maps were computed as the angle between the principal diffusion direction v1 and B_0. The 3D T_1- and T_2-weighted scans were acquired with the following sequences: 3D T_1-weighted scan: acquired voxel size = 1.0 × 1.0 × 1.6 mm^3, reconstructed voxel = 0.8 × 0.8 × 0.8 mm^3, TR/TE = 7.6/3.7 ms, and FOV = 256 × 256 × 160 mm^3. 3D T_2-weighted scan: acquired voxel size = 1.0 × 1.0 × 1.6 mm^3, reconstructed voxel = 0.8 × 0.8 × 0.8 mm^3, TR/TE = 2500/363 ms, and FOV = 256 × 256 × 160 mm^3. The combination $(T_1 — T_2) / (T_1 + T_2)$ of the T_1- and T_2-weighted scans has enhanced contrast between WM, GM and subcortical structures[33], and was used for tissue segmentation with FSL's FAST. For DGM, we manually defined every structure using SWI and FA images. All WM masks were eroded with a 4 × 4 × 4 mm^3 kernel prior to further analysis. In MS patients, focal lesions were excluded from the R_2^* analysis. These lesions were manually defined based on both T_1-weighted images and the combination $(T_1 — T_2) / (T_1 + T_2)$. Thresholding WM via fractional anisotropy (FA) was avoided because FA is known to change in the non-lesional WM of patients with MS[34,35]. For each subject, all voxels with orientations within 5-degree intervals around a given angle θ were pooled to calculate the average R_2^* relaxation rate. The numerical R_2^* model was then fitted to each individual $R_2^*(\theta)$-curve. An a priori decision was made to exclude subjects if best fits were too poor (adjusted $R^2 < 0.70$).

Fitting the Tissue Model to in vivo Human Data

Input parameters for a best fit with the experimental data were determined through a gradient descent based L2-norm minimization algorithm using MATLAB's *lsqcurvefit* (NLLS, Matlab 2014b). Weighted fits were performed on previously published experimental $R_2^*(\theta)$ data acquired in healthy controls, subjects with MS, and healthy siblings of subjects with MS, with weights corresponding to the number of voxels in a given fibre orientation angle bin[20]. The lowest number of voxels are for fibre bundles parallel to the direction of B_0 (0°), with increasing number of voxels for increasing angles. Note that this difference in the number of voxels is not a feature of the brain but a mere geometrical effect. For any given direction, the number of fibre bundles is lowest parallel to the direction[9]. In all three groups, myelin volume fraction (MVF) and iron concentration were chosen as varying parameters. To model myelin content as a continuous variable, the axons' g-ratio was used as a measure of myelin content. The MVF was allowed to vary between 11.0% to 25.3% for non-lesional WM, while iron concentration was permitted to vary from 15 to 65 mg of iron/kg of fresh tissue, with an initial assumption of 42.4 mg/kg for healthy iron concentration in WM[15]. The corresponding myelin water fraction (MWF) was obtained by halving the MVF. Best fits were chosen on the basis of highest coefficient of determination (adjusted R^2).

Statistical Analysis

Statistical analysis was performed using R (lmerTest and lsmeans Package). To account for age as a covariate, linear regression analysis was performed to determine relations between individual parameters (MVF and iron concentration) and age. For both acquired parameters, a one-way analysis of covariance (ANCOVA), with age accounted for, was conducted for simultaneous comparison between the three cohorts (patients, siblings, controls). In cases where the parameters were determined by ANCOVA to be significantly different ($p < 0.05$) between all 3 groups, a subsequent Bonferroni-Holm was performed to correct for Type I error. We assessed the differences in the mean iron concentration and MVF values across the three cohorts.

Fit of an Empirical Model to $R_2^*(\theta)$ simulated with the Numerical Tissue Model

Lee and colleagues[11] have proposed an empirical model for R_2^* in WM

$$\mathrm{R}_2^*(\theta, MWF) = c_0 + c_1 \cdot MWF + c_2 \cdot MWF \cdot cos(2\theta) + c_3 \cdot MWF \cdot \cos(4\theta) \qquad (6)$$

where MWF denotes the myelin water fraction, c_0 is a myelin-independent and orientation-independent contribution to $R_2^*(\theta)$, c_1 is the orientation-independent contribution of myelin, and c_2 and c_3 are orientation-dependent contributions of myelin. We simulated $R_2^*(\theta)$ for different iron and myelin concentrations using our numerical model, and fitted Equation 6 to the resulting simulated data. Coefficients c_0 and c_2 were chosen as varying parameters, while c_1 and c_3 were kept fixed at 0.17 and 0.025, respectively, as previously determined[11]. We investigated the behaviour of the myelin-independent and orientation-independent coefficient c_0 as a function of the simulated iron concentrations. The MVF in a range based on the minimum MVF and maximum MVF values previously predicted from best fits to human data, with increments of 0.2%. For each MVF value, a total of 5 different iron concentration values were simulated (range from 0 to 60 mg/kg, with intervals of 12 mg/kg). A linear regression was then fitted to the c_0 versus iron concentration function to determine a linear regression coefficient. This was repeated for all simulated MVF and the final linear regression coefficient for iron was obtained by averaging the individual coefficients. This resultant linear regression coefficient is the simulated iron-dependent slope that relates the myelin-independent and orientation-independent contribution of $R_2^*(\theta)$, c_0, to a global average iron content in NAWM. To check normality, a Kolmogorov-Smirnov test[36] was applied on the distribution of iron-dependent slopes.

Phantom Data

A phantom containing 24 different concentrations of BSA (A2153, Sigma-Aldrich; Vienna, Austria) and ferritin from equine spleen (F4503, Sigma-Aldrich; Vienna Austria) was generated to mimic variations of iron and myelin content similar to brain tissue[37]. The four weight fractions of BSA relative to water were 0.14, 0.18, 0.22 and 0.26. Ferritin was varied from 0 to 150 mg of iron/kg of fresh tissue, with 6 increments of 25 mg/kg. 2D GRE data of the phantom were acquired at 37°C[24] on a 3T scanner (Tim Trio; Siemens Healthcare, Erlangen, Germany), with TE = 4.7, 10.51, 16.1, 21.69, 27.28 ms, TR = 470 ms, and flip angle = 15°. To reach the desired temperature, the phantom was flushed with water at 37°C prior to data acquisition, using a water pump and a heating device to maintain constant temperature. To prevent flow artifacts, the water pump was switched off during scanning. R_2^* was calculated voxel-wise by a mono-exponential fit to the decay data. R_2^* was analyzed in circular regions of interest (ROI) in each tube. For each BSA concentration, a linear regression was fitted to obtain the linear relationship between measured R_2^* and actual iron concentration, referred to as the experimental iron concentration dependent slope.

Results

Simulations of Various Contents of Myelin and Iron for the Numerical Tissue Model

Numerical simulations for different concentrations of myelin and iron in WM are shown in Figure 2. The red curve with markers corresponds to a plausible situation in healthy subjects, assuming 17.32%

MVF and 43.1 mg/kg iron. Here, $R_2^*(\theta)$ ranged from $R_2^*(0^o) = 21.17\ s^{-1}$ to $R_2^*(90^o) = 23.13\ s^{-1}$ (difference in R_2^* between 0^o and 90^o $\Delta R_2^* = 1.96\ s^{-1}$). This $R_2^*(\theta)$ cannot be simulated without contributions from iron. A simulation without iron but with the same ΔR_2^* results in an overall R_2^* that is too low, ranging from $R_2^*(0^o) = 16.67\ s^{-1}$ to $R_2^*(90^o) = 18.64\ s^{-1}$. On the other hand, a simulation without iron that matches $R_2^*(0^o)$ results in an unrealistically high MVF of 53.92% and an excessive orientation dependency. In general, simulations with non-zero but low iron content that match $R_2^*(0^o)$ result in myelin concentrations that are too high. Lastly, a realistic MVF of 17.32% and an iron concentration of 0 mg/kg results in a realistic orientation dependence but an overall R_2^* that is too low.

Fitting the Numerical Model to in vivo Human Data

Best fits to the individual $R_2^*(\theta)$ curves of each subject yielded distributions of iron concentration and MVF (Table 2, Figures 3 and 4). A total of 34 (out of 39) subjects with MS, 28 (out of 31) healthy siblings of MS patients, and 29 (out of 30) healthy controls yielded best fits with coefficients of determination $R^2 > 0.70$. Iron concentration was found to be highest in healthy siblings of MS patients, while the MVF was comparable between healthy controls and siblings. Conversely, the MS group was found to have the lowest MVF and iron concentration. Upon performing an ANCOVA with Bonferroni-Holm correction for all three cohorts, the averaged iron concentration remained significantly increased in healthy siblings of MS patients relative to controls ($p = 0.039$) and significantly decreased in MS patients, when compared to controls ($p = 0.0016$) and healthy siblings ($p < 0.0001$). Averaged MVF was found to be significantly lower in MS patients ($p = 0.0019$), relative to healthy siblings of MS patients. Compared with the unrelated control group, no significant difference in MVF was found in healthy siblings ($p = 0.13$) and MS patients ($p = 0.072$). Using the averages of myelin and iron contents obtained from the fits (Table 2), average $R_2^*(\theta)$ curves were computed and compared with the averages of the *in vivo* $R_2^*(\theta)$ curves. The adjusted coefficients of determination were $R^2 = 0.95$ for unrelated healthy controls, $R^2 = 0.95$ for healthy siblings of MS patients, and $R^2 = 0.93$ for MS patients.

Fitting the Empirical $R_2^*(\theta)$ Model to $R_2^*(\theta)$ simulated with the Numerical Tissue Model

The MVF of the numerical model was varied from 12.20% to 25.10% with increments of 0.2% to produce 69 different MVF values. This range was chosen based on the maximum MVF of 25.23% and minimum MVF of 12.12% obtained by fitting the numerical model to the human data (Table 2). For the linear regression fit to the coefficient c_0 versus iron concentration (IC) function, an averaged regression coefficient of 0.081 ± 0.002 s^{-1} per mg iron per kg tissue and an intercept of 17.19 ± 0.41 s^{-1} were obtained. The adjusted coefficient of determinations ranged from $R^2 = 0.80$ to 0.99, with mean adjusted $R^2 = 0.94 \pm 0.06$. Values of all 69 iron-dependent slopes, as predicted by the Kolmogorov-Smirnov test, appear to be normally distributed ($p > 0.15$). Substituting these results into the model by Lee et al. described in Eq. (6), we obtain an extended model that also incorporates iron concentration

$$\mathrm{R}_2^*(\theta, MWF, IC) = 17.19 + 0.081 \cdot IC + c_1 \cdot MWF + c_2 \cdot MWF \cdot cos(2\theta) + c_3 \cdot MWF \cdot cos(4\theta), \qquad (7)$$

where c_0 splits into an IC-independent constant and an IC-dependent component.

Phantom

Both an increase in BSA and ferritin result in an increase in R_2^* (Figure 5). The linear regression yielded adjusted R^2 between 0.97 and 0.99. A BSA concentration of 0.14 approximately mimics *in vivo* WM properties[37]. For an iron concentration of 43 mg/kg and 0.14 BSA to water per weight, R_2^* becomes 22.6 s^{-1}, which is similar to *in vivo* WM R_2^*. The slopes of R_2^*([Fe]) increase with increasing BSA concentrations ranging from 0.100 ± 0.007 s^{-1} per mg iron per kg tissue at 0.14 BSA (green line with circles) to 0.147 ± 0.009 s^{-1} per mg iron per kg tissue at 0.26 BSA (red line with triangles). Given the linear relation between R_2^* and iron concentration for different BSA concentrations, a single value for R_2^* may result from various combinations of values for iron and BSA concentration. An R_2^* of 30 s^{-1}, for instance, may correspond to a mix of 60 mg/kg iron and 0.18 BSA, or to an iron concentration 118 mg/kg and 0.14 BSA. For a single measurement of R_2^*, there is no unique value for iron and BSA concentration. Furthermore, the experimental iron-dependent slope of 0.100 ± 0.007 s^{-1} per mg iron per kg tissue determined for 0.14 BSA provides a basis of comparison with the simulated iron-dependent slope of 0.081 ± 0.002 s^{-1} per mg iron per kg tissue.

Discussion

In this work, we propose a numerical tissue model to describe R_2^* in human WM. Furthermore, we performed an orientation-independent phantom experiment, which showed that there is no unique solution of ferritin and BSA concentrations that match a given R_2^*. By exploiting the orientation dependency of WM R_2^* *in vivo*, which originates from the axons' macroscopic anisotropy and the orientation-dependent magnetic susceptibility of myelin, it is possible to compute a unique solution of average MVF and iron concentration in healthy or non-lesional WM, provided that the fibre orientation is known. The contribution of iron to R_2^* was explored and explicitly included in a previously proposed empirical model of R_2^*. The orientation-independent phantom experiment then provided data in support of the empirical model's expansion.

In WM of the healthy human brain, non-heme iron is stored in ferritin proteins and predominately found in oligodendrocytes, the cells which form the myelin sheaths and utilize catalytic iron for myelin production[38]. Therefore, a tight connection between iron and myelin content has to be assumed in WM. Myelin loss in MS is not only found in focally demyelinated lesions, but also extends to non-lesional WM[21,39,40]. Primarily, loss of myelin lipids rather than myelin proteins characterizes non-lesional myelin loss, which occurs more diffusely than myelin loss within MS lesions[41]. Furthermore, a widespread decrease of iron in NAWM[23] and in focal lesions[42] has been shown to relate to disease duration[23]. In agreement with these findings, our data showed that compared to controls, both iron and myelin in non-lesional WM are reduced in MS patients. In a matched cohort of healthy siblings of patients with MS, on the other hand, our results suggest a significant increase in WM iron by 4.7 mg/kg of tissue. Although siblings of patients with MS have an increased likelihood of developing MS due to a similar genetic background and comparable environmental risk factors[43], the sibling cohort in our study, at an average age of 50 years, was older than the typical average age of MS onset. These siblings are therefore quite unlikely to actually develop MS. It has been suggested that oxidative stress due to increased iron content is a further risk factor for MS[44–46]. While this potential risk factor may still be present in the sibling cohort in the form of an increased WM iron content prior to any disease manifestations, other risk factors may be absent. Previous studies have reported radiological differences in siblings of MS patients compared to controls[47,48]. In the present study, subjects with radiological abnormalities, such as WM hyperintensities on FLAIR images, were excluded from the two healthy cohorts.

Assuming a myelin water content of 50%, the MVF of 17.32% in controls, 18.19% in siblings, and 16.02% in patients translate to MWFs of 8.66%, 9.10%, and 8.01%, respectively. These concentrations are in good agreement with previous studies using myelin water imaging[49–51]. The values are also in good agreement with a conversion between MWF and MVF presented recently[52]. Note, however, that myelin not only affects the R_2^* of myelin water but all water in the vicinity of myelin. Even without myelin water, myelin would have an effect on $R_2^*(\theta)$, since it induces non-local field inhomogeneities that reach well beyond the space occupied by myelin water. The range of both iron and myelin content is in agreement with literature values. For iron, Hallgren and Sourander report a standard deviation of 8.8 mg per kg WM tissue in subjects with an age range of 30 to 100 years. While WM iron plateaus after the age of 35[15], myelin is known to decrease with healthy aging[53,54], leading to a range of myelin concentrations in healthy adults of different ages. Vavasour et al. reported a MWF of 8.9 ± 1.0% in NAWM of MS patients, which is in good agreement the MVF of 16.02 ± 2.07% in our patient cohort[40].

By computing $R_2^*(\theta)$, spatial information is lost. In return, the ability to fit an orientation-dependent model to the acquired R_2^* data is gained, providing a unique solution for the average global WM myelin and iron content. Since diffuse damage appears to accompany disease progression in MS[21], quantitative whole WM estimates for iron and/or myelin may be sensitive markers for disease progression. If this is the case, the scan for R_2^* mapping would be readily available on most current MRI scanners. Such approach would be clinically attractive because it provides simple quantitative whole WM estimates for average myelin and iron content. Further correlation with clinical data[55] or biochemical data, such as serum ferritin levels[56] would be straightforward. Note also that 3D gradient echo MRI will likely become part of routine imaging protocols for MS, as it is required for the detection of the central vein sign as a diagnostic marker for MS[57–61]. Lastly, this approach may also be sensitive to diffuse WM-wide remyelination rendered possible by future treatment approaches for MS, and may complement measures of remyelination in focal lesions using magnetization transfer imaging[62], myelin water imaging[28,63,64], or MR phase based approaches[65,66].

This work has some limitations. While the model yields realistic myelin and iron estimates, it should be kept in mind that these values are averages across the entire WM and regional variations of myelin and iron are not captured. For a particular voxel, the tissue composition is not known and variations between different brain areas are to be expected. By pooling voxels from across the entire WM, these regional differences are averaged out and $R_2^*(\theta)$ becomes accessible, allowing for the determination of realistic myelin and iron concentrations with high adjusted R^2, albeit at the loss of spatial information.
However, for fibre tracts that cover a sufficiently large range of orientations, it may be possible to obtain tract-specific concentrations of myelin and iron. Such measurements may be aided by acquisitions at different head orientations, but clinical feasibility of such approach would be limited. Furthermore, since we avoided using an FA threshold for the selection of WM, voxels with low FA and

poorly defined local fibre orientation were included in the analysis and averaged with other voxels. Voxels with crossing fibres pose challenges to the model as well as to the analysis. Crossing fibres may be present in voxels measured across all fibre orientations, and may subsequently be measured as an orientation-independent $R_2^*(\theta)$ contribution. By fitting the numerically obtained $R_2^*(\theta)$ curves to *in vivo* $R_2^*(\theta)$, the model may overestimate iron content and underestimate myelin content due to the presence of crossing fibres. Nevertheless, this is primarily a result of the diffusion acquisition techniques of fibre orientation in *in vivo* data, and not of the efficacy of the numerical model. Advanced diffusion scans, such as diffusion basis spectrum imaging[67] and higher spatial resolution would alleviate some of the issues by reducing the proportion of voxels with crossing fibres. Furthermore, in MS lesions with profound axonal loss, the tissue orientation is also ill-defined. However, there was almost no difference in $R_2^*(\theta)$ when lesions were included or excluded[20]. This finding suggests that the step of lesion exclusion may be omitted for the investigation of non-lesional WM in MS using the proposed approach. Since MS is associated with atrophy of about 0.5% per year[68,69], the question arises on how the proposed approach is affected by tissue loss. Brain atrophy in MS is well studied, and its quantification was suggested to aid clinical assessment of MS[68]. While atrophy may target certain structures more than others, it is agnostic to the angle between fibres and B_0 during an MRI scan. With atrophy, the averaging that leads to the $R_2^*(\theta)$ curve happens across a smaller number of voxels, which reduces the signal-to-noise ratio but does not affect the overall shape of the $R_2^*(\theta)$ curve. Atrophy would have to target a) a certain angle range and b) a certain R_2^* within that angle range in order to distort the $R_2^*(\theta)$ curve. This would be a highly unnatural process.

We provide additional insight on the iron related c_0 coefficient of an empirical model for $R_2^*(\theta)$[11], with a clear correlation displayed between coefficient c_0 and iron concentration. By including an iron-dependent slope of 0.081 ± 0.002 s^{-1} per mg iron per kg tissue, it may become possible to disentangle the contributions of iron from overall $R_2^*(\theta)$, with the remaining constant offset describing other tissue contributions to R_2^*. The obtained slope is in good agreement with the slope of 0.100 ± 0.007 s^{-1} at 0.14 BSA measured in the phantom, and with the slope of 0.100 s^{-1} per mg iron per kg tissue reported for WM in a previous post-mortem study[1].

For the numerical model, several assumptions and simplifications were made:

1. We kept the number of simulated axons fixed and used the g-ratio to control the amount of myelin, in order for myelin content to vary as a continuous variable. With only a few axons within the simulated volume, it is not possible to control myelin content via e.g. myelinated versus non-myelinated axons or the total number of axons. The g-ratios corresponding to the best fits have therefore no direct biological meaning and were converted to myelin content.

2. For ferritin, we assumed that all ferritin molecules are loaded with the same number of 4500 iron atoms. In reality, ferritin is mostly loaded with fewer than 4500 iron atoms[70]. Therefore, the iron content determined with our approach may not be translated to a number of ferritin molecules.

3. Only a small piece of WM was simulated due to high computational cost. The reasons are that ferritin and axons have length scales that differ by three orders of magnitude and that the simulation has to be performed in three dimensions.

4. For similar reasons, we did not include vasculature in the model, which is another two orders of magnitude larger than axons. A considerable proportion of the blood resides in blood vessels that run in parallel with WM tracts[71], causing a tissue orientation effect in gradient echo dynamic susceptibility contrast perfusion MRI[72,73]. Veins should therefore also contribute to R_2^* in an orientation-dependent manner. However, the total blood volume in WM is only about 2.6%[74], resulting in a venous WM blood volume of less than 2%. Moreover, the blood volume in NAWM of patients with MS is only marginally lower relative to controls[75].

5. Diffusion of the proton spins was not taken into account and the signal loss was assumed to be dominated by static dephasing. The diffusion lengths in the experimental data are much larger than the characteristic lengths of the field inhomogeneities produced by both ferritin and axons[26], suggesting that motional narrowing may have an impact on R_2^*. With static dephasing, the model fit to an individual subject takes about half a day on a typical personal computer (Intel i7, 32 GB of memory). The modelling of diffusion effects would increase the computational cost by at least two orders of magnitude, making the fitting of a total of 91 subjects computationally infeasible. Even without modelling diffusion-mediated effects, we can see that iron-induced contributions are required to fit to experimental R_2^* measured in WM. Furthermore, the iron-dependent slope derived from the phantom

experiment (0.100 ± 0.007 s^{-1} per mg iron per kg) is in close agreement to the slope derived from the static simulation (0.081 ± 0.002 s^{-1} per mg iron per kg). This implies that regardless of a static model or a model with diffusion, the contributions of iron on overall R_2^* are additive, and independent of whether diffusion is modelled.

6. By fitting a mono-exponential decay to the multi echo data, we neglected the multi-exponential nature of R_2^* relaxation, which cannot be captured with a scan that only has 5 echoes.

7. We kept the T_2 of myelin water, intracellular and extracellular water constant between the three cohorts. This simplification seems justified in a regime that is dominated by static dephasing.

In conclusion, we presented an approach for estimating average global non-lesional myelin and iron content from orientation-dependent R_2^* data. Application of the proposed numerical tissue model to *in vivo* data shows significant loss of iron and myelin in subjects with MS, in line with histopathological reports, and a significant increase in iron in healthy siblings of subjects with MS. The proposed approach may be useful for the assessment of disease progression in MS.

Funding

This study was funded by NSERC (016-05371) and the National MS Society (RG-1507-05031). D. Kor and J. Doucette were funded by NSERC USRA (USRA 513103-2017, USRA 527378-2018, and USRA 497681-2016). C. Birkl was funded by the Austrian Science Fund (J4038-B27). V. Wiggermann was supported by a graduate studentship award from the MS Society of Canada (EGID 2002). A. Rauscher is funded by Canada Research Chairs.

References

1. Langkammer C, Krebs N, Goessler W, et al. Quantitative MR imaging of brain iron: a postmortem validation study. *Radiology*. 2010;257(2):455-462.

2. Walsh AJ, Blevins G, Lebel RM, Seres P, Emery DJ, Wilman AH. Longitudinal MR Imaging of Iron in Multiple Sclerosis: An Imaging Marker of Disease. *Radiology*. August 2013.

3. Walsh AJ, Lebel RM, Eissa A, et al. Multiple sclerosis: validation of MR imaging for quantification and detection of iron. *Radiology*. 2013;267(2):531-542.

4. Khalil M, Langkammer C, Pichler A, et al. Dynamics of brain iron levels in multiple sclerosis: A longitudinal 3T MRI study. *Neurology*. 2015;84(24):2396-2402.

5. Khalil M, Langkammer C, Ropele S, et al. Determinants of brain iron in multiple sclerosis: a quantitative 3T MRI study. *Neurology*. 2011;77(18):1691-1697.

6. Schweser F, Raffaini Duarte Martins AL, Hagemeier J, et al. Mapping of thalamic magnetic susceptibility in multiple sclerosis indicates decreasing iron with disease duration: A proposed mechanistic relationship between inflammation and oligodendrocyte vitality. *NeuroImage*. 2018;167:438-452.

7. Hernández-Torres E, Wiggermann V, Machan L, et al. Increased mean R2* in the deep gray matter of multiple sclerosis patients: Have we been measuring atrophy? *J Magn Reson Imaging*. 0(0).

8. Bender B, Klose U. The in vivo influence of white matter fiber orientation towards B(0) on T2* in the human brain. *NMR Biomed*. 2010;23(9):1071-1076.

9. Denk C, Hernandez Torres E, MacKay A, Rauscher A. The influence of white matter fibre orientation on MR signal phase and decay. *NMR Biomed*. 2011;24(3):246-252.

10. Lee J, van Gelderen P, Kuo L-W, Merkle H, Silva AC, Duyn JH. T2*-based fiber orientation mapping. *NeuroImage*. 2011;57(1):225-234.

11. Lee J, Shin H-G, Jung W, Nam Y, Oh S-H, Lee J. An R2* model of white matter for fiber orientation and myelin concentration. *NeuroImage*. 2017;162:269-275.

12. Oh S-H, Kim Y-B, Cho Z-H, Lee J. Origin of B0 orientation dependent R2(*) (=1/T2(*)) in white matter. *NeuroImage*. 2013;73:71-79.

13. Xu T, Foxley S, Kleinnijenhuis M, Chen WC, Miller KL. The effect of realistic geometries on the susceptibility-weighted MR signal in white matter. *Magn Reson Med*. 2018;79(1):489-500.

14. Wharton S, Bowtell R. Fiber orientation-dependent white matter contrast in gradient echo MRI. *Proc Natl Acad Sci U S A*. 2012;109(45):18559-18564.

15. HALLGREN B, SOURANDER P. The effect of age on the non-haemin iron in the human brain. *J Neurochem*. 1958;3(1):41-51.

16. Krebs N, Langkammer C, Goessler W, et al. Assessment of trace elements in human brain using inductively coupled plasma mass spectrometry. *J Trace Elem Med Biol Organ Soc Miner Trace Elem GMS*. 2014;28(1):1-7.

17. Filippi M, Bozzali M, Rovaris M, et al. Evidence for widespread axonal damage at the earliest clinical stage of multiple sclerosis. *Brain J Neurol*. 2003;126(Pt 2):433-437.

18. Tortorella C, Viti B, Bozzali M, et al. A magnetization transfer histogram study of normal-appearing brain tissue in MS. *Neurology*. 2000;54(1):186-193.

19. Laule C, Vavasour IM, Moore GRW, et al. Water content and myelin water fraction in multiple sclerosis. A T2 relaxation study. *J Neurol*. 2004;251(3):284-293.

20. Hernández-Torres E, Wiggermann V, Hametner S, et al. Orientation Dependent MR Signal Decay Differentiates between People with MS, Their Asymptomatic Siblings and Unrelated Healthy Controls. *PLoS ONE*. 2015;10(10):e0140956.

21. Kutzelnigg A, Lucchinetti CF, Stadelmann C, et al. Cortical demyelination and diffuse white matter injury in multiple sclerosis. *Brain*. 2005;128(11):2705-2712.

22. Haider L, Zrzavy T, Hametner S, et al. The topograpy of demyelination and neurodegeneration in the multiple sclerosis brain. *Brain J Neurol*. 2016;139(Pt 3):807-815.

23. Hametner S, Wimmer I, Haider L, Pfeifenbring S, Bruck W, Lassmann H. Iron and neurodegeneration in the multiple sclerosis brain. *Ann Neurol*. 2013;74(6):848-861.

24. Birkl C, Langkammer C, Krenn H, et al. Iron mapping using the temperature dependency of the magnetic susceptibility. *Magn Reson Med*. 2015;73(3):1282-1288.

25. Deistung A, Schweser F, Reichenbach JR. Overview of quantitative susceptibility mapping. *NMR Biomed*. July 2016.

26. Duyn JH, Schenck J. Contributions to magnetic susceptibility of brain tissue. *NMR Biomed*. 2017;30(4).

27. Liu C. Susceptibility tensor imaging. *Magn Reson Med Off J Soc Magn Reson Med Soc Magn Reson Med*. 2010;63(6):1471-1477.

28. Mackay A, Whittall K, Adler J, Li D, Paty D, Graeb D. <I>In vivo</I> visualization of myelin water in brain by magnetic resonance. *Magn Reson Med*. 1994;31(6):673-677.

29. Harrison PM, Arosio P. The ferritins: molecular properties, iron storage function and cellular regulation. *Biochim Biophys Acta BBA - Bioenerg*. 1996;1275(3):161-203.

30. Trapp BD, Kidd GJ. Chapter 1 - Structure of the Myelinated Axon. In: *Myelin Biology and Disorders*. San Diego: Academic Press; 2004:3-27.

31. Schenck JF. Magnetic resonance imaging of brain iron. *J Neurol Sci*. 2003;207(1-2):99-102.

32. Jenkinson M, Beckmann CF, Behrens TEJ, Woolrich MW, Smith SM. FSL. *NeuroImage*. 2012;62(2):782-790.

33. Misaki M, Savitz J, Zotev V, et al. Contrast enhancement by combining T1- and T2-weighted structural brain MR Images. *Magn Reson Med*. 2015;74(6):1609-1620.

34. Roosendaal SD, Geurts JJG, Vrenken H, et al. Regional DTI differences in multiple sclerosis patients. *NeuroImage*. 2009;44(4):1397-1403.

35. Kim S-H, Kwak K, Hyun J-W, et al. Diffusion tensor imaging of normal-appearing white matter in patients with neuromyelitis optica spectrum disorder and multiple sclerosis. *Eur J Neurol*. 2017;24(7):966-973.

36. Öner M, Kocakoç İD. JMASM 49: A Compilation of Some Popular Goodness of Fit Tests for Normal Distribution: Their Algorithms and MATLAB Codes (MATLAB). *J Mod Appl Stat Methods*. 2017;16(2).

37. Soellinger M, Langkammer C, Seifert-Held T, Fazekas F, Ropele S. Fast bound pool fraction mapping using stimulated echoes. *Magn Reson Med*. 2011;66(3):717-724.

38. Todorich B, Pasquini JM, Garcia CI, Paez PM, Connor JR. Oligodendrocytes and myelination: The role of iron. *Glia*. October 2008.

39. Bagnato F, Hametner S, Boyd E, et al. Untangling the R2* contrast in multiple sclerosis: A combined MRI-histology study at 7.0 Tesla. *PloS One*. 2018;13(3):e0193839.

40. Vavasour IM, Huijskens SC, Li DK, et al. Global loss of myelin water over 5 years in multiple sclerosis normal-appearing white matter. *Mult Scler Houndmills Basingstoke Engl*. August 2017:1352458517723717.

41. Laule C, Pavlova V, Leung E, et al. Diffusely abnormal white matter in multiple sclerosis: further histologic studies provide evidence for a primary lipid abnormality with neurodegeneration. *J Neuropathol Exp Neurol*. 2013;72(1):42-52.

42. Wiggermann V, Hametner S, Hernández-Torres E, et al. Susceptibility-sensitive MRI of multiple sclerosis lesions and the impact of normal-appearing white matter changes. *NMR Biomed*. 2017;30(8):e3727.

43. Chao MJ, Barnardo MCNM, Lincoln MR, et al. HLA class I alleles tag HLA-DRB1*1501 haplotypes for differential risk in multiple sclerosis susceptibility. *Proc Natl Acad Sci U S A*. 2008;105(35):13069-13074.

44. Haider L, Fischer MT, Frischer JM, et al. Oxidative damage in multiple sclerosis lesions. *Brain*. 2011;134(7):1914-1924.

45. Lassmann H, van Horssen J. Oxidative stress and its impact on neurons and glia in multiple sclerosis lesions. *Biochim Biophys Acta*. 2016;1862(3):506-510.

46. Levine SM. The Role of Iron in the Pathogenesis of Experimental Allergic Encephalomyelitis and Multiple Sclerosis. *N Y Acad Sci Ann*. 2004;1012:252-266.

47. Xia Z, Steele SU, Bakshi A, et al. Assessment of Early Evidence of Multiple Sclerosis in a Prospective Study of Asymptomatic High-Risk Family Members. *JAMA Neurol*. 2017;74(3):293-300.

48. Gabelic T, Ramasamy DP, Weinstock-Guttman B, et al. Prevalence of radiologically isolated syndrome and white matter signal abnormalities in healthy relatives of patients with multiple sclerosis. *AJNR Am J Neuroradiol*. 2014;35(1):106-112.

49. Groeschel S, Hagberg GE, Schultz T, et al. Assessing White Matter Microstructure in Brain Regions with Different Myelin Architecture Using MRI. *PLOS ONE*. 2016;11(11):e0167274.

50. Meyers SM, Kolind SH, MacKay AL. Simultaneous measurement of total water content and myelin water fraction in brain at 3T using a T2 relaxation based method. *Magn Reson Imaging*. 2017;37:187-194.

51. Meyers SM, Laule C, Vavasour IM, et al. Reproducibility of myelin water fraction analysis: a comparison of region of interest and voxel-based analysis methods. *Magn Reson Imaging*. April 2009.

52. Jung W, Lee J, Shin H-G, et al. Whole brain g-ratio mapping using myelin water imaging (MWI) and neurite orientation dispersion and density imaging (NODDI). *NeuroImage*. September 2017.

53. Peters A. The effects of normal aging on myelin and nerve fibers: A review. *J Neurocytol*. 2002;31(8):581-593.

54. Wiggins RC, Gorman A, Rolsten C, Samorajski T, Ballinger WE, Freund G. Effects of aging and alcohol on the biochemical composition of histologically normal human brain. *Metab Brain Dis*. 1988;3(1):67-80.

55. Cohen RA, Kessler HR, Fischer M. The Extended Disability Status Scale (EDSS) as a predictor of impairments of functional activities of daily living in multiple sclerosis. *J Neurol Sci*. 1993;115(2):132-135.

56. Sfagos C, Makis AC, Chaidos A, et al. Serum ferritin, transferrin and soluble transferrin receptor levels in multiple sclerosis patients. *Mult Scler Houndmills Basingstoke Engl*. 2005;11(3):272-275.

57. Sati P, Oh J, Constable RT, et al. The central vein sign and its clinical evaluation for the diagnosis of multiple sclerosis: a consensus statement from the North American Imaging in Multiple Sclerosis Cooperative. *Nat Rev Neurol*. 2016;12(12):714-722.

58. Maggi P, Absinta M, Grammatico M, et al. Central vein sign differentiates Multiple Sclerosis from central nervous system inflammatory vasculopathies. *Ann Neurol*. 2018;83(2):283-294.

59. Mistry N, Abdel-Fahim R, Samaraweera A, et al. Imaging central veins in brain lesions with 3-T T2*-weighted magnetic resonance imaging differentiates multiple sclerosis from microangiopathic brain lesions. *Mult Scler J*. 2016;22(10):1289-1296.

60. Samaraweera APR, Clarke MA, Whitehead A, et al. The Central Vein Sign in Multiple Sclerosis Lesions Is Present Irrespective of the T2* Sequence at 3 T. *J Neuroimaging*. 2017;27(1):114-121.

61. Samaraweera APR, Falah Y, Pitiot A, Dineen RA, Morgan PS, Evangelou N. The MRI central vein marker; differentiating PPMS from RRMS and ischemic SVD. *Neurol Neuroimmunol Neuroinflammation*. 2018;5(6):e496.

62. Ropele S, Fazekas F. Magnetization Transfer MR Imaging in Multiple Sclerosis. *Neuroimaging Clin N Am*. 2009;19(1):27-36.

63. Laule C, Kozlowski P, Leung E, Li DKB, MacKay AL, Moore GRW. Myelin water imaging of multiple sclerosis at 7 T: correlations with histopathology. *NeuroImage*. 2008;40(4):1575-80.

64. Prasloski T, Rauscher A, MacKay AL, et al. Rapid whole cerebrum myelin water imaging using a 3D GRASE sequence. *NeuroImage*. 2012;63(1):533-539.

65. Wiggermann V, Hametner S, Hernández-Torres E, et al. Cover Image, Volume 30, Issue 8. *NMR Biomed*. 2017;30(8):i-i.

66. Wiggermann V, Hernández Torres E, Vavasour IM, et al. Magnetic resonance frequency shifts during acute MS lesion formation. *Neurology*. 2013;81(3):211-218.

67. Wang Y, Wang Q, Haldar JP, et al. Quantification of increased cellularity during inflammatory demyelination. *Brain J Neurol*. 2011;134(Pt 12):3590-3601.

68. Rocca MA, Battaglini M, Benedict RHB, et al. Brain MRI atrophy quantification in MS: From methods to clinical application. *Neurology*. 2017;88(4):403-413.

69. Zivadinov R, Jakimovski D, Gandhi S, et al. Clinical relevance of brain atrophy assessment in multiple sclerosis. Implications for its use in a clinical routine. *Expert Rev Neurother*. 2016;16(7):777-793.

70. Brooks RA, Vymazal J, Goldfarb RB, Bulte JW, Aisen P. Relaxometry and magnetometry of ferritin. *Magn Reson Med*. 1998;40(2):227-235.

71. Okudera T, Huang YP, Fukusumi A, Nakamura Y, Hatazawa J, Uemura K. Micro-angiographical studies of the medullary venous system of the cerebral hemisphere. *Neuropathol Off J Jpn Soc Neuropathol*. 1999;19(1):93-111.

72. Hernández-Torres E, Kassner N, Forkert ND, et al. Anisotropic cerebral vascular architecture causes orientation dependency in cerebral blood flow and volume measured with dynamic susceptibility contrast magnetic resonance imaging. *J Cereb Blood Flow Metab Off J Int Soc Cereb Blood Flow Metab*. June 2016.

73. Doucette J, Wei L, Hernández-Torres E, et al. Rapid solution of the Bloch-Torrey equation in anisotropic tissue: Application to dynamic susceptibility contrast MRI of cerebral white matter. *NeuroImage*. 2018;185:198-207.

74. Leenders KL, Perani D, Lammertsma AA, et al. Cerebral blood flow, blood volume and oxygen utilization. Normal values and effect of age. *Brain J Neurol*. 1990;113 (Pt 1):27-47.

75. Lapointe E, Li DKB, Traboulsee AL, Rauscher A. What Have We Learned from Perfusion MRI in Multiple Sclerosis? *AJNR Am J Neuroradiol*. January 2018.

Figure Captions

Figure 1: An example of the magnetic field inhomogeneities generated by myelinated axons and ferritin computed using equation 5. For this example, the tissue model was oriented at an angle of 90º relative to the main magnetic field.

Figure 2: Simulated $R_2^*(\theta)$ curves for different iron and myelin volume fractions. The red curve with markers corresponds to typical R_2^* measured in volunteers at 3T. Due to the orientation dependency of myelin related R_2^*, this curve cannot be obtained with myelin alone (green dashed, yellow dashed, purple solid line). Without iron, the orientation dependency may be qualitatively the same as in the measured data, but the overall R_2^* is too low (yellow and green dashed lines). On the other hand, with a myelin content that results in the correct R_2^* at low angles, the orientation dependency (ΔR_2^*) is too large (purple solid). $R_2^*(\theta)$ curves with different combinations of iron and myelin content have been simulated (green, blue and orange solid). Relative to the optimal simulated R_2^* curve (red solid with markers), these curves have the same R_2^* at low angles. At higher angles, however, the curves deviate significantly from the realistic simulated R_2^* curve, due to the high myelin contents needed to achieve realistic $R_2^*(0^o)$ values.

Figure 3: (A) All simulated curves (solid lines) with fitted parameters overlaid on experimental R_2^* data (points) with patients with MS in green, healthy siblings of patients with MS in blue and unrelated healthy controls in red. (B, C and D): The simulated curves from the individual cohorts of healthy controls, siblings of MS patients, and MS patients, respectively.

Figure 4: Iron concentration and myelin volume fraction (MVF) values for all three groups computed by fitting the numerical model. Coloured dots represent the fitted parameters for individual curves grouped in either MS patients (green), healthy siblings of MS patients (blue) and unrelated healthy controls (red). Significant differences in iron concentration were observed with comparisons between healthy siblings of MS patients and unrelated healthy controls ($p = 0.039$), between unrelated healthy

controls and MS patients ($p = 0.0016$), and between healthy siblings of MS patients and MS patients ($p < 0.0001$). For MVF values, significant differences were observed with the comparison between healthy siblings of MS patients and MS patients ($p = 0.0019$). However, the comparison between unrelated healthy controls and healthy siblings of MS patients yielded no significant difference in MVF ($p = 0.17$), and remained insignificant even without the Bonferroni-Holm correction. Although no significant difference in MVF ($p = 0.072$) was observed the comparison between unrelated healthy controls and MS patients, it should be noted that all reported p-values are corrected for Type I error via the Bonferroni-Holm method. Pairwise comparison between MS patients and unrelated healthy controls yielded an uncorrected $p = 0.036$.

Figure 5: R_2^* measured in a phantom of 24 different concentrations of BSA and ferritin (iron). R_2^* values increase with increasing concentrations of BSA and ferritin. For a single value of measured R_2^*, several combinations of BSA and iron concentration are possible.

Tables

	MS Patients	**Siblings of MS patients**	**Healthy Controls**
N (female/male)	39 (35/4)	31 (20/11)	30 (25/5)
Age (years)	[32 – 69] (49.7 ± 10.1)	[30 – 67] (50.6 ± 11.0)	[30 – 67] (50.6 ± 11.3)
Age at disease onset (years)	[17 – 56] (32.4 ± 8.0)	N/A	N/A
Disease Duration (DD, years)	[3 – 41] (17.2 ± 9.3)	N/A	N/A
Expanded disability status scale	[0 – 6.5] median 2.5	N/A	N/A

Table 1: The demographic of subjects across all three cohorts.

	Iron Concentration [range] (mean ± STD) [mg/kg]	**Myelin Volume Fraction [range] (mean ± STD) [%]**	**Adjusted R^2 [range] (mean ± STD)**
Controls	[27.9 - 57.2] (43.1 ± 8.3)	[12.92 - 22.84] (17.32 ± 2.20)	[0.84 - 0.99] (0.94 ± 0.04)
Siblings	[31.4 - 61.0] (47.8 ± 8.2)	[14.50 - 25.23] (18.19 ± 2.98)	[0.70 - 0.99] (0.93 ± 0.07)
Patients	[15.7 - 50.7] (35.6 ± 8.9)	[12.12 - 20.11] (16.02 ± 2.07)	[0.76 - 0.99] (0.93 ± 0.05)

Table 2: The distribution of fitted parameters for all three groups with their corresponding coefficients of determination. Relative to unrelated healthy controls, significantly increased mean iron concentration was found in healthy siblings of MS patients. Significantly decreased mean iron concentration was found in MS patients compared to the other two groups. Relative to healthy siblings of MS patients, significantly decreased myelin volume fraction was found in MS patients.

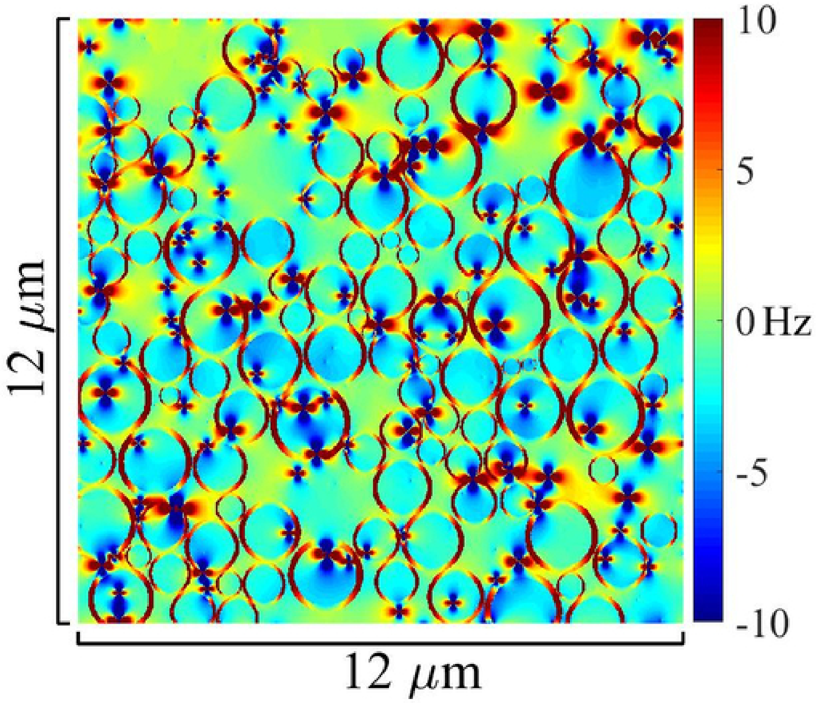

Figure 1: An example of the magnetic field inhomogeneities generated by myelinated axons and ferritin computed using equation 5. For this example, the tissue model was oriented at an angle of 90° relative to the main magnetic field.

26x23mm (600 x 600 DPI)

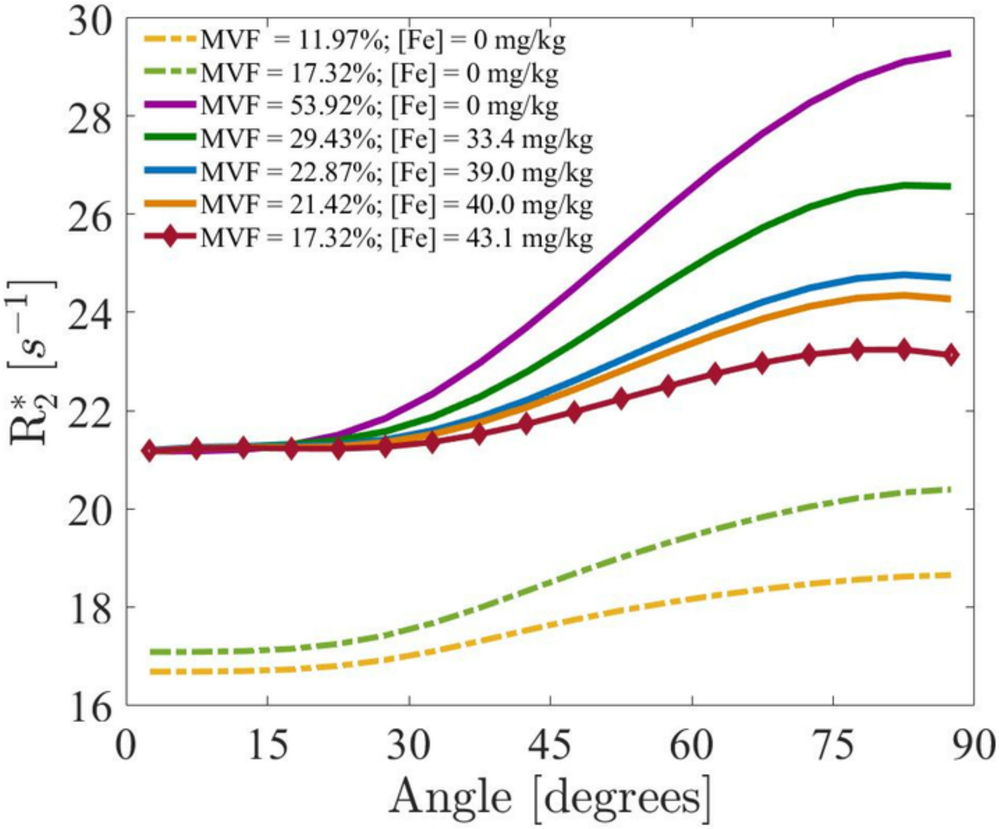

Figure 2: Simulated $R_2^*(\theta)$ curves for different iron and myelin volume fractions. The red curve with markers corresponds to typical R_2^* measured in volunteers at 3T. Due to the orientation dependency of myelin related R_2^*, this curve cannot be obtained with myelin alone (green dashed, yellow dashed, purple solid line). Without iron, the orientation dependency may be qualitatively the same as in the measured data, but the overall R_2^* is too low (yellow and green dashed lines). On the other hand, with a myelin content that results in the correct R_2^* at low angles, the orientation dependency (ΔR_2^*) is too large (purple solid). $R_2^*(\theta)$ curves with different combinations of iron and myelin content have been simulated (green, blue and orange solid). Relative to the optimal simulated R_2^* curve (red solid with markers), these curves have the same R_2^* at low angles. At higher angles, however, the curves deviate significantly from the realistic simulated R_2^* curve, due to the high myelin contents needed to achieve realistic $R_2^*(0^o)$ values.

30x27mm (600 x 600 DPI)

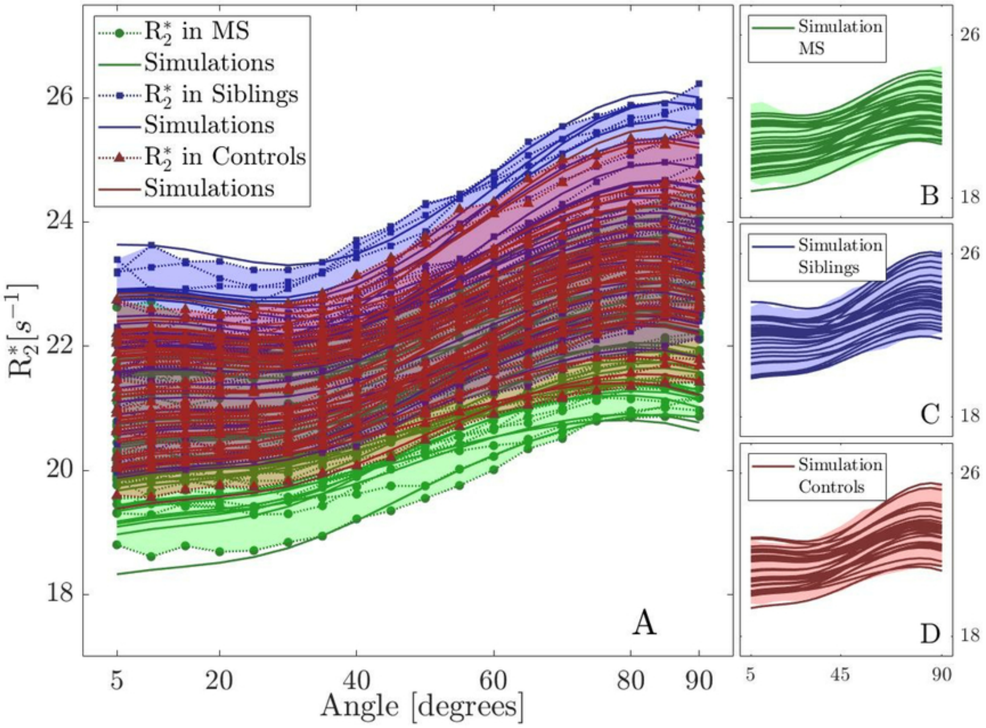

Figure 3: (A) All simulated curves (solid lines) with fitted parameters overlaid on experimental R_2^* data (points) with patients with MS in green, healthy siblings of patients with MS in blue and unrelated healthy controls in red. (B, C and D): The simulated curves from the individual cohorts of healthy controls, siblings of MS patients, and MS patients, respectively.

37x27mm (600 x 600 DPI)

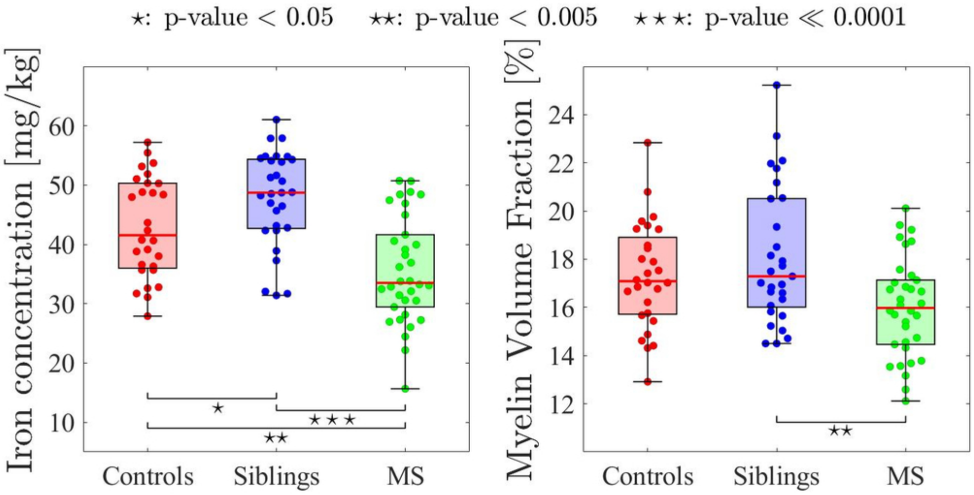

Figure 4: Iron concentration and myelin volume fraction (MVF) values for all three groups computed by fitting the numerical model. Coloured dots represent the fitted parameters for individual curves grouped in either MS patients (green), healthy siblings of MS patients (blue) and unrelated healthy controls (red). Significant differences in iron concentration were observed with comparisons between healthy siblings of MS patients and unrelated healthy controls ($p = 0.039$), between unrelated healthy controls and MS patients ($p = 0.0016$), and between healthy siblings of MS patients and MS patients ($p < 0.0001$). For MVF values, significant differences were observed with the comparison between healthy siblings of MS patients and MS patients ($p = 0.0019$). However, the comparison between unrelated healthy controls and healthy siblings of MS patients yielded no significant difference in MVF ($p = 0.17$), and remained insignificant even without the Bonferroni-Holm correction. Although no significant difference in MVF ($p = 0.072$) was observed the comparison between unrelated healthy controls and MS patients, it should be noted that all reported p-values are corrected for Type I error via the Bonferroni-Holm method. Pairwise comparison between MS patients and unrelated healthy controls yielded an uncorrected $p = 0.036$.

43x23mm (600 x 600 DPI)

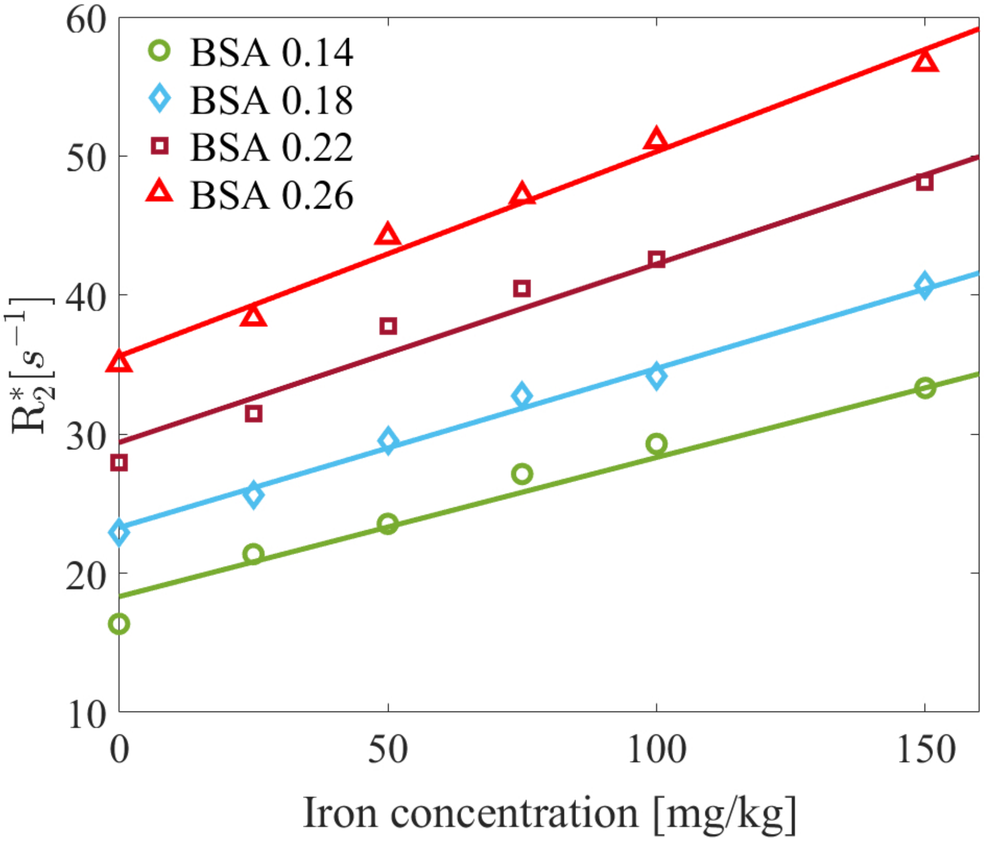

Figure 5: $R_2{}^*$ measured in a phantom of 24 different concentrations of BSA and ferritin (iron). $R_2{}^*$ values increase with increasing concentrations of BSA and ferritin. For a single value of measured $R_2{}^*$, several combinations of BSA and iron concentration are possible.

A computational model, which incorporates iron content, myelin content and fibre orientation to simulate R_2^* decay in white matter, is proposed. Applying the model to fibre orientation dependent *in vivo* R_2^* data, we were able to determine a unique solution of myelin and iron content in global white matter, with significantly increased iron content in healthy siblings of MS patients. We demonstrate that a model combining myelin-induced orientation-dependent and iron-induced orientation-independent components is able to fit *in vivo* R_2^* data.

	Iron Concentration [range] (mean ± STD) [mg/kg]	**Myelin Volume Fraction [range] (mean ± STD) [%]**	**Adjusted R^2 [range] (mean ± STD)**
Controls	[27.9 - 57.2] (43.1 ± 8.3)	[12.92 - 22.84] (17.32 ± 2.20)	[0.84 - 0.99] (0.94 ± 0.04)
Siblings	[31.4 - 61.0] (47.8 ± 8.2)	[14.50 - 25.23] (18.19 ± 2.98)	[0.70 - 0.99] (0.93 ± 0.07)
Patients	[15.7 - 50.7] (35.6 ± 8.9)	[12.12 - 20.11] (16.02 ± 2.07)	[0.76 - 0.99] (0.93 ± 0.05)

⋆: $p\text{-value} < 0.05$ ⋆⋆: $p\text{-value} < 0.01$

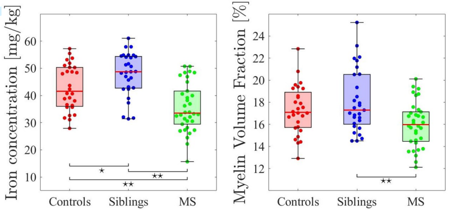

The role of iron and myelin in orientation dependent R_2^* of white matter

D. Kor, C. Birkl, S. Ropele, J. Doucette, T. Xu, V. Wiggermann, E. Hernández-Torres, S. Hametner and A.Rauscher...xx-xx

The role of iron and myelin in orientation dependent R_2^* of white matter

Daniel Kor[1,2], Christoph Birkl[2,3,4], Stefan Ropele[4], Jonathan Doucette[1,2,3], Tianyou Xu[5], Vanessa Wiggermann[1,2,3], Enedino Hernández-Torres[2,3], Simon Hametner[6], Alexander Rauscher[1,2,3,7]

[1] Department of Physics & Astronomy, University of British Columbia, Vancouver, BC, Canada
[2] UBC MRI Research Centre, University of British Columbia, Vancouver, BC, Canada
[3] Department of Pediatrics (Division of Neurology), University of British Columbia, Vancouver, BC, Canada
[4] Department of Neurology, Medical University of Graz, Graz, Austria
[5] Oxford Centre for Functional MRI of the Brain, University of Oxford, Oxford, United Kingdom
[6] Institute of Neuropathology, University Medical Center Göttingen, Göttingen, Germany
[7]Department of Radiology, University of British Columbia, Vancouver, BC, Canada

Corresponding Author
Daniel Kor
Department of Physics and Astronomy
UBC MRI Research Centre

University of British Columbia
M10 - Purdy Pavilion
2221 Wesbrook Mall
Vancouver, BC V6T 2B5
E-mail: daniel.kor@alumni.ubc.ca
Tel: +1 604 827 5462
Fax: +1 604 827 3339

Word count: 5,543

Keywords: MRI; R_2^*; white matter fibre orientation; brain iron; myelin; multiple sclerosis; neurodegenerative disease; susceptibility-weighted imaging

Short title: Iron and myelin in orientation dependent R_2^*

Abbreviation used: WM, white matter; MVF, myelin volume fraction; MC, myelin content characterized by myelin water fraction; MWF, myelin water fraction; IC, iron concentration

Abstract

Brain myelin and iron content are important parameters in neurodegenerative diseases such as multiple sclerosis (MS). Both myelin and iron content influence the brain's R_2^* relaxation rate. However, their quantification based on R_2^* maps requires a realistic tissue model that can be fitted to the measured data. In structures with low myelin content, such as deep gray matter, R_2^* shows a linear increase with increasing iron content. In white matter, R_2^* is not only affected by iron and myelin but also by the orientation of the myelinated axons with respect to the external magnetic field. Here, we propose a numerical model which incorporates iron and myelin, as well as fibre orientation, to simulate R_2^* decay in white matter. Applying our model to fibre orientation-dependent *in vivo* R_2^* data, we are able to determine a unique solution of myelin and iron content in global white matter. We determine an averaged myelin volume fraction of 16.02 ± 2.07% in non-lesional white matter of patients with MS, 17.32 ± 2.20% in matched healthy controls, and 18.19 ± 2.98% in healthy siblings of patients with MS. Averaged iron content was 35.6 ± 8.9 mg/kg tissue in patients, 43.1 ± 8.3 mg/kg in controls, and 47.8 ± 8.2 mg/kg in siblings. <u>All differences in iron content between groups were significant, while the difference in myelin content between MS patients and the siblings of MS patients was significant.</u> In conclusion, we demonstrate that a model that combines myelin-induced orientation-dependent and iron-induced orientation-independent components is able to fit *in vivo* R_2^* data. R1.1

Introduction

In the human brain, diamagnetic myelin and paramagnetic iron are major contributors to the magnetic resonance signal's R_2^* relaxation rate. In deep gray matter (DGM), post mortem studies have shown that R_2^* correlates well with tissue iron concentrations[1–3]. Therefore, R_2^* is widely used as an *in vivo* imaging measure for DGM iron[4–7]. In the white matter (WM), the situation is more complicated. Measured R_2^* relaxation in WM depends not only on the tissue composition but also on the angle θ between WM fibre tracts and the main magnetic field B_0[8–13]. This orientation dependency has been attributed to the magnetic field inhomogeneities generated by the structural anisotropy of WM tracts and the anisotropic magnetic susceptibility of myelin itself[11,13,14]. While DGM structures have the highest iron concentrations of up to 240 mg iron per kg tissue, WM contains about 30 to 45 mg iron per kg of tissue[15,16].

The radiological hallmarks of multiple sclerosis (MS) are hyperintense WM lesions on T_2-weighted MRI. In addition to focal demyelinated WM lesions, diffuse alteration of the non-lesional WM has been observed when using various MR methodologies, such as proton MR spectroscopy[17], magnetization transfer ratio[18], myelin water imaging[19], or R_2^* in combination with diffusion tensor imaging (DTI). By associating a measured R_2^* with a fibre orientation, θ, computed from DTI, the orientation dependent $R_2^*(\theta)$ can be calculated[20]. R1.2 Histopathological studies have revealed diffuse and extensive damage in the normal appearing white matter (NAWM), encompassing myelin loss, axonal injury, microglia activation, and perivascular inflammatory infiltrates[21,22]. In MS, NAWM iron was found to be gradually reduced over the course of the disease[23], possibly accompanying the loss of myelin[21]. These pathological findings offer an explanation on why $R_2^*(\theta)$ differs significantly between patients with MS, healthy controls, and healthy siblings of patients with MS[20]. Therefore, there is clinical interest in quantifying both myelin and iron in the entire WM from MRI data. However, myelin and iron both increase R_2^*. An approach to separate the contribution of iron and myelin to R_2^* is to measure temperature-dependent R_2^*, which is however restricted to post mortem studies[24]. While quantitative susceptibility mapping[25] is able to distinguish paramagnetic (e.g. iron) from diamagnetic (e.g. myelin) susceptibility sources, it does not distinguish myelin loss from iron increase, as both lead to an increase in magnetic susceptibility[26].

The behaviour of the magnetic susceptibility of myelin is described by a tensor[14]. Consequently, myelin induces a modification on the local magnetic field that depends on the angle between the myelinated axon and the main magnetic field, B_0[14,27]. Since iron is predominantly stored in ferritin, a protein shell with an approximately spherical biomineral core, its modifications on the local magnetic field are orientation-independent[11]. This key difference between myelin sheaths and iron cores opens another avenue for the interrogation of tissue myelin and iron with MRI via the orientation dependency of R_2^*. Such an approach requires a model describing how R_2^* depends on these two quantities and the axons' orientation relative to B_0.

Here, we present a numerical tissue model that considers contributions from orientation-dependent myelin and orientation-independent iron. With this model, we compute orientation-dependent R_2^* from first principles. By fitting the modelled $R_2^*(\theta)$ curves to experimental data, we obtain global averages for iron and myelin contents in non-lesional WM of patients with MS, healthy siblings of patients, and unrelated healthy controls. The findings obtained from the numerical tissue model are then put into context with a previous R_2^* model[11]. Finally, by acquiring data in an orientation-independent phantom at varying combinations of diamagnetic bovine serum albumin (BSA) and paramagnetic ferritin concentrations, we explore how these two substances influence R_2^*, albeit in an orientation-independent manner.

Theory

Numerical Tissue Model

Myelinated axons and ferritin were modelled as cylinders and spheres, respectively. Axon sizes were modelled as a gamma distribution around a mean radius of 0.46 μm, with the distribution's shape parameter of 3.82, and assigned a packing density of approximately 64%[13]. For a 3T external magnetic field, a T_2 relaxation time of 15 ms was assumed for myelin water, and 63 ms for intracellular and extracellular water[28]. Each ferritin molecule was allocated a radius of 4 nm, with the sphere assumed to be filled with 4500 ferric ions[29]. Subvoxels containing ferritin were assigned a T_2 relaxation time of 0.001 ms, which is arbitrary but effectively leads to zero transverse magnetization. Myelin g-ratio and the iron concentration were left as free-varying parameters. For the simulation, the myelin sheath, which is related to myelin g-ratio, was assumed to consist of 50% water[30]. Due to the presence of ferritin, there is no cylindrical symmetry and the tissue had to be modelled in three dimensions. The ferritin molecules were randomly distributed throughout a plane centred at the simulated volume, to ensure that the magnetic field inhomogeneities generated by the ferritin were captured by the simulation volume. The intra-axonal and extra-axonal spaces were assigned a reference magnetic susceptibility of $\chi = 0$, with all other magnetic susceptibilities relative to this reference value. The magnetic susceptibility of the ferritin was assumed to be a scalar with $\chi_f = 520$ ppm[26,31]. In tensor notation, this is represented as a diagonal matrix with identical entries:

$$\chi_{ferritin} = \begin{bmatrix} \chi_f & 0 & 0 \\ 0 & \chi_f & 0 \\ 0 & 0 & \chi_f \end{bmatrix}. \tag{1}$$

The magnetic susceptibility of myelin is a rank 2 tensor:

$$\chi_{myelin} = \begin{bmatrix} \chi_i + \chi_a & 0 & 0 \\ 0 & \chi_i - \frac{\chi_a}{2} & 0 \\ 0 & 0 & \chi_i - \frac{\chi_a}{2} \end{bmatrix}, \tag{2}$$

where isotropic magnetic susceptibility of myelin is χ_i = -60 ppb and its anisotropic magnetic susceptibility is χ_a = -120 ppb[14]. To produce a simulated three-dimensional magnetic susceptibility map χ of a WM tissue voxel, the tissue compartments were assigned the magnetic susceptibilities of myelin, ferritin, as well as intra- and extra-axonal water. Prior to magnetic field computation, a coordinate transformation was performed on χ to obtain the magnetic susceptibility map in the common reference frame of the axon, χ_R:

$$\chi_R(r,\phi) = R(\phi) \cdot \chi \cdot R(\phi)^T, \tag{3}$$

where the magnetic susceptibility values are now dependent on their spatial position, defined by radial coordinate r and azimuthal coordinate ϕ, relative to the axon and R is the rotation matrix defined as:

$$R(\phi) = \begin{bmatrix} cos(\phi) & sin(\phi) & 0 \\ -sin(\phi) & cos(\phi) & 0 \\ 0 & 0 & 1 \end{bmatrix}, \tag{4}$$

The magnetic field created by this configuration was then forward calculated in the Fourier domain via Equation 5, as derived in[27]:

$$\Delta f(r,\phi) = FT^{-1}\left\{\frac{1}{3}\hat{\mathrm{H}}^{\mathrm{T}} FT\left\{\chi_R(r,\phi)\right\}\hat{\mathrm{H}} - \hat{\mathrm{H}}^{\mathrm{T}}\mathrm{k}\frac{\mathrm{k}^{\mathrm{T}} FT\left\{\chi_R(r,\phi)\right\}\hat{\mathrm{H}}}{\mathrm{k}^2}\right\}\gamma\mathrm{H}, \qquad (5)$$

where $\Delta f(r,\phi)$ is the off resonance frequency in Hz, $\chi_R(r,\phi)$ denotes the spatial susceptibility tensor matrix defined relative to the reference frame of the axon, γ is the gyromagnetic ratio, FT is the Fourier Transform and FT^{-1} is the inverse Fourier Transform. The vectors $\hat{H} = [\sin(\theta), 0, \cos(\theta)]$ and $k = [kx, ky, kz]$ represent the unit direction vector of the external magnetic field and the spatial frequency vector, respectively, where θ represents the fibre orientation relative to the external magnetic field. In the simulation, the external magnetic field, H, is assumed to be 3T. For isotropic magnetic susceptibility, the tensor becomes a diagonal matrix and the forward calculation becomes a convolution with a unit dipole kernel. An illustration of the magnetic field inhomogeneities generated by the model's geometry is shown in Figure 1.

Model

The geometry of the model for both ferritin and axons spans length scales across three orders of magnitude. The myelinated axons and ferritin were simulated on a 600 × 600 × 60 array of subvoxels that corresponds to a $2.4 \times 2.4 \times 0.24\ \mu m^3$ volume. A spatial resolution of 4 nm per subvoxel was used, following the observation of numerical rounding artifacts when simulating at the initially decided spatial resolution of 8 nm.

For any given fibre orientation between 0 and 90 degrees (in 5-degree intervals), the transverse magnetization within the 3D volume was simulated for a multi-gradient echo signal up to 100 ms in steps of 5 ms. For a given echo time, the signal was computed by taking the magnitude of the integral over the complex signals in the 600 × 600 × 60 subvoxels. Note that the phase evolution during these 5 ms intervals may be more than 2π, but when computing the signal, we are only interested in the subvoxels' phase at a certain time and not how many 2π revolutions have happened until then. A single exponential was then fitted to the computed signal decay in order to simulate R_2^*.

In vivo Human Data

The numerical myelin-ferritin model described in Section *Model* was applied to $R_2^*(\theta)$ of 39 subjects with MS, 31 healthy siblings of subjects with MS, and 30 healthy unrelated controls (see Table 1 for demographic details) published previously[20]. All subjects gave their written informed consent according to the Declaration of Helsinki. All subjects were scanned on a 3T system (Philips Achieva) using an 8-channel SENSE head coil. Data for R_2^* maps were acquired with a three dimensional gradient echo sequence with five echoes (TR = 28 ms, TE_1 = 5 ms, echo spacing = 5 ms, acquired voxel size = 0.9 × 1.0 × 1.6 mm^3, reconstructed voxel = 0.8 × 0.8 × 0.8 mm^3). R_2^* maps were calculated by fitting a mono-exponential function to the signal decay in each voxel. Diffusion tensor imaging (DTI) data were collected with a spin echo planar sequence (b0 = 0, b1 = 1000, 16 directions, TR/TE = 7465/75 ms, FOV = 212 × 212 mm^2, 60 slices of 2.2 mm thickness, in-plane resolution = 2.2 × 2.2 mm^2). DTI data were analyzed using FSL[32] and fibre orientation maps were computed as the angle between the principal diffusion direction v1 and B_0. The 3D T_1- and T_2-weighted scans were acquired with the following sequences: 3D T_1-weighted scan: acquired voxel size = 1.0 × 1.0 × 1.6 mm^3, reconstructed voxel = 0.8 × 0.8 × 0.8 mm^3, TR/TE = 7.6/3.7 ms, and FOV = 256 × 256 × 160 mm^3. 3D T_2-weighted scan: acquired voxel size = 1.0 × 1.0 × 1.6 mm^3, reconstructed voxel = 0.8 × 0.8 × 0.8 mm^3, TR/TE = 2500/363 ms, and FOV = 256 × 256 × 160 mm^3. The combination $(T_1 — T_2) / (T_1 + T_2)$ of the T_1- and T_2-weighted scans has enhanced contrast between WM, GM and subcortical structures[33], and was used for tissue segmentation with FSL's FAST. For DGM, we manually defined every structure using SWI and FA images. R1.3 All WM masks were eroded with a 4 × 4 × 4 mm^3 kernel prior to further analysis. In MS patients, focal lesions were excluded from the R_2^* analysis. These lesions were manually defined based on both T_1-weighted images and the combination $(T_1 — T_2) / (T_1 + T_2)$. Thresholding WM via fractional anisotropy (FA) was avoided because FA is known to change in the non-lesional WM of patients with MS[34,35]. For each subject, all voxels with orientations within 5-degree intervals around a given angle θ were pooled to calculate the average R_2^* relaxation rate. The numerical R_2^* model was then fitted to each individual $R_2^*(\theta)$-curve. An a priori decision was made to exclude subjects if best fits were too poor (adjusted $R^2 < 0.70$).

Fitting the Tissue Model to in vivo Human Data

Input parameters for a best fit with the experimental data were determined through a gradient descent based L2-norm minimization algorithm using MATLAB's *lsqcurvefit* (NLLS, Matlab 2014b). Weighted fits were performed on previously published experimental $R_2^*(\theta)$ data acquired in healthy controls, subjects with MS, and healthy siblings of subjects with MS, with weights corresponding to the number of voxels in a given fibre orientation angle bin[20]. The lowest number of voxels are for fibre bundles parallel to the direction of B_0 (0°), with increasing number of voxels for increasing angles. Note that this difference in the number of voxels is not a feature of the brain but a mere geometrical effect. For any given direction, the number of fibre bundles is lowest parallel to the direction[9]. In all three groups, myelin volume fraction (MVF) and iron concentration were chosen as varying parameters. To model myelin content as a continuous variable, the axons' g-ratio was used as a measure of myelin content. The MVF was allowed to vary between 11.0% to 25.3% for non-lesional WM, while iron concentration was permitted to vary from 15 to 65 mg of iron/kg of fresh tissue, with an initial assumption of 42.4 mg/kg for healthy iron concentration in WM[15]. The corresponding myelin water fraction (MWF) was obtained by halving the MVF. Best fits were chosen on the basis of highest coefficient of determination (adjusted R^2).

Statistical Analysis

Statistical analysis was performed using R (lmerTest and lsmeans Package). To account for age as a covariate, linear regression analysis was performed to determine relations between individual parameters (MVF and iron concentration) and age. For both acquired parameters, a one-way analysis of covariance (ANCOVA), with age accounted for, was conducted for simultaneous comparison between the three cohorts (patients, siblings, controls). In cases where the parameters were determined by ANCOVA to be significantly different ($p < 0.05$) between all 3 groups, a subsequent Bonferroni-Holm was performed to correct for Type I error. We assessed the differences in the mean iron concentration and MVF values across the three cohorts.

Fit of an Empirical Model to $R_2^*(\theta)$ simulated with the Numerical Tissue Model

Lee and colleagues[11] have proposed an empirical model for R_2^* in WM

$$\mathrm{R}_2^*(\theta, MWF) = c_0 + c_1 \cdot MWF + c_2 \cdot MWF \cdot cos(2\theta) + c_3 \cdot MWF \cdot \cos(4\theta) \qquad (6)$$

where MWF denotes the myelin water fraction, c_0 is a myelin-independent and orientation-independent contribution to $R_2^*(\theta)$, c_1 is the orientation-independent contribution of myelin, and c_2 and c_3 are orientation-dependent contributions of myelin. We simulated $R_2^*(\theta)$ for different iron and myelin concentrations using our numerical model, and fitted Equation 6 to the resulting simulated data. Coefficients c_0 and c_2 were chosen as varying parameters, while c_1 and c_3 were kept fixed at 0.17 and 0.025, respectively, as previously determined[11]. We investigated the behaviour of the myelin-independent and orientation-independent coefficient c_0 as a function of the simulated iron concentrations. The MVF in a range based on the minimum MVF and maximum MVF values previously predicted from best fits to human data, with increments of 0.2%. For each MVF value, a total of 5 different iron concentration values were simulated (range from 0 to 60 mg/kg, with intervals of 12 mg/kg). A linear regression was then fitted to the c_0 versus iron concentration function to determine a linear regression coefficient. This was repeated for all simulated MVF and the final linear regression coefficient for iron was obtained by averaging the individual coefficients. This resultant linear regression coefficient is the simulated iron-dependent slope that relates the myelin-independent and orientation-independent contribution of $R_2^*(\theta)$, c_0, to a global average iron content in NAWM. To check normality, a Kolmogorov-Smirnov test[36] was applied on the distribution of iron-dependent slopes.

Phantom Data

A phantom containing 24 different concentrations of BSA (A2153, Sigma-Aldrich; Vienna, Austria) and ferritin from equine spleen (F4503, Sigma-Aldrich; Vienna Austria) was generated to mimic variations of iron and myelin content similar to brain tissue[37]. The four weight fractions of BSA relative to water were 0.14, 0.18, 0.22 and 0.26. Ferritin was varied from 0 to 150 mg of iron/kg of fresh tissue, with 6 increments of 25 mg/kg. 2D GRE data of the phantom were acquired at 37°C[24] on a 3T scanner (Tim Trio; Siemens Healthcare, Erlangen, Germany), with TE = 4.7, 10.51, 16.1, 21.69, 27.28 ms, TR = 470 ms, and flip angle = 15°. To reach the desired temperature, the phantom was flushed with water at 37°C prior to data acquisition, using a water pump and a heating device to maintain constant temperature. To prevent flow artifacts, the water pump was switched off during scanning. R_2^* was calculated voxel-wise by a mono-exponential fit to the decay data. R_2^* was analyzed in circular regions of interest (ROI) in each tube. For each BSA concentration, a linear regression was fitted to obtain the linear relationship between measured R_2^* and actual iron concentration, referred to as the experimental iron concentration dependent slope.

Results

Simulations of Various Contents of Myelin and Iron for the Numerical Tissue Model

Numerical simulations for different concentrations of myelin and iron in WM are shown in Figure 2. The red curve with markers corresponds to a plausible situation in healthy subjects, assuming 17.32%

MVF and 43.1 mg/kg iron. Here, $R_2^*(\theta)$ ranged from $R_2^*(0^o) = 21.17\ s^{-1}$ to $R_2^*(90^o) = 23.13\ s^{-1}$ (difference in R_2^* between 0° and 90° $\Delta R_2^* = 1.96\ s^{-1}$). This $R_2^*(\theta)$ cannot be simulated without contributions from iron. A simulation without iron but with the same ΔR_2^* results in an overall R_2^* that is too low, ranging from $R_2^*(0^o) = 16.67\ s^{-1}$ to $R_2^*(90^o) = 18.64\ s^{-1}$. On the other hand, a simulation without iron that matches $R_2^*(0^o)$ results in an unrealistically high MVF of 53.92% and an excessive orientation dependency. In general, simulations with non-zero but low iron content that match $R_2^*(0^o)$ result in myelin concentrations that are too high. Lastly, a realistic MVF of 17.32% and an iron concentration of 0 mg/kg results in a realistic orientation dependence but an overall R_2^* that is too low.

Fitting the Numerical Model to in vivo Human Data

Best fits to the individual $R_2^*(\theta)$ curves of each subject yielded distributions of iron concentration and MVF (Table 2, Figures 3 and 4). A total of 34 (out of 39) subjects with MS, 28 (out of 31) healthy siblings of MS patients, and 29 (out of 30) healthy controls yielded best fits with coefficients of determination $R^2 > 0.70$. Iron concentration was found to be highest in healthy siblings of MS patients, while the MVF was comparable between healthy controls and siblings. Conversely, the MS group was found to have the lowest MVF and iron concentration. Upon performing an ANCOVA with Bonferroni-Holm correction for all three cohorts, the averaged iron concentration remained significantly increased in healthy siblings of MS patients relative to controls ($p = 0.039$) and significantly decreased in MS patients, when compared to controls ($p = 0.0016$) and healthy siblings ($p < 0.0001$). Averaged MVF was found to be significantly lower in MS patients ($p = 0.0019$), relative to healthy siblings of MS patients. Compared with the unrelated control group, no significant difference in MVF was found in healthy siblings ($p = 0.13$) and MS patients ($p = 0.072$). Using the averages of myelin and iron contents obtained from the fits (Table 2), average $R_2^*(\theta)$ curves were computed and compared with the averages of the *in vivo* $R_2^*(\theta)$ curves. The adjusted coefficients of determination were $R^2 = 0.95$ for unrelated healthy controls, $R^2 = 0.95$ for healthy siblings of MS patients, and $R^2 = 0.93$ for MS patients.

Fitting the Empirical $R_2^*(\theta)$ Model to $R_2^*(\theta)$ simulated with the Numerical Tissue Model

The MVF of the numerical model was varied from 12.20% to 25.10% with increments of 0.2% to produce 69 different MVF values. This range was chosen based on the maximum MVF of 25.23% and minimum MVF of 12.12% obtained by fitting the numerical model to the human data (Table 2). For the linear regression fit to the coefficient c_0 versus iron concentration (IC) function, an averaged regression coefficient of 0.081 ± 0.002 s^{-1} per mg iron per kg tissue and an intercept of 17.19 ± 0.41 s^{-1} were obtained. The adjusted coefficient of determinations ranged from $R^2 = 0.80$ to 0.99, with mean adjusted $R^2 = 0.94 \pm 0.06$. Values of all 69 iron-dependent slopes, as predicted by the Kolmogorov-Smirnov test, appear to be normally distributed ($p > 0.15$). Substituting these results into the model by Lee et al. described in Eq. (6), we obtain an extended model that also incorporates iron concentration

$$\mathrm{R}_2^*(\theta, MWF, IC) = 17.19 + 0.081 \cdot IC + c_1 \cdot MWF + c_2 \cdot MWF \cdot cos(2\theta) + c_3 \cdot MWF \cdot cos(4\theta), \tag{7}$$

where c_0 splits into an IC-independent constant and an IC-dependent component.

Phantom

Both an increase in BSA and ferritin result in an increase in R_2^* (Figure 5). The linear regression yielded adjusted R^2 between 0.97 and 0.99. A BSA concentration of 0.14 approximately mimics *in vivo* WM properties[37]. For an iron concentration of 43 mg/kg and 0.14 BSA to water per weight, R_2^* becomes 22.6 s^{-1}, which is similar to *in vivo* WM R_2^*. The slopes of R_2^*([Fe]) increase with increasing BSA concentrations ranging from 0.100 ± 0.007 s^{-1} per mg iron per kg tissue at 0.14 BSA (green line with circles) to 0.147 ± 0.009 s^{-1} per mg iron per kg tissue at 0.26 BSA (red line with triangles). Given the linear relation between R_2^* and iron concentration for different BSA concentrations, a single value for R_2^* may result from various combinations of values for iron and BSA concentration. An R_2^* of 30 s^{-1}, for instance, may correspond to a mix of 60 mg/kg iron and 0.18 BSA, or to an iron concentration 118 mg/kg and 0.14 BSA. For a single measurement of R_2^*, there is no unique value for iron and BSA concentration. Furthermore, the experimental iron-dependent slope of 0.100 ± 0.007 s^{-1} per mg iron per kg tissue determined for 0.14 BSA provides a basis of comparison with the simulated iron-dependent slope of 0.081 ± 0.002 s^{-1} per mg iron per kg tissue.

Discussion

In this work, we propose a numerical tissue model to describe R_2^* in human WM. Furthermore, we performed an orientation-independent phantom experiment, which showed that there is no unique solution of ferritin and BSA concentrations that match a given R_2^*. By exploiting the orientation dependency of WM R_2^* *in vivo*, which originates from the axons' macroscopic anisotropy and the orientation-dependent magnetic susceptibility of myelin, it is possible to compute a unique solution of average MVF and iron concentration in healthy or non-lesional WM, provided that the fibre orientation is known. The contribution of iron to R_2^* was explored and explicitly included in a previously proposed empirical model of R_2^*. The orientation-independent phantom experiment then provided data in support of the empirical model's expansion.

In WM of the healthy human brain, non-heme iron is stored in ferritin proteins and predominately found in oligodendrocytes, the cells which form the myelin sheaths and utilize catalytic iron for myelin production[38]. Therefore, a tight connection between iron and myelin content has to be assumed in WM. Myelin loss in MS is not only found in focally demyelinated lesions, but also extends to non-lesional WM[21,39,40]. Primarily, loss of myelin lipids rather than myelin proteins characterizes non-lesional myelin loss, which occurs more diffusely than myelin loss within MS lesions[41]. Furthermore, a widespread decrease of iron in NAWM[23] and in focal lesions[42] has been shown to relate to disease duration[23]. In agreement with these findings, our data showed that compared to controls, both iron and myelin in non-lesional WM are reduced in MS patients. In a matched cohort of healthy siblings of patients with MS, on the other hand, our results suggest a significant increase in WM iron by 4.7 mg/kg of tissue. Although siblings of patients with MS have an increased likelihood of developing MS due to a similar genetic background and comparable environmental risk factors[43], the sibling cohort in our study, at an average age of 50 years, was older than the typical average age of MS onset. These siblings are therefore quite unlikely to actually develop MS. It has been suggested that oxidative stress due to increased iron content is a further risk factor for MS[44–46]. While this potential risk factor may still be present in the sibling cohort in the form of an increased WM iron content prior to any disease manifestations, other risk factors may be absent. Previous studies have reported radiological differences in siblings of MS patients compared to controls[47,48]. In the present study, subjects with radiological abnormalities, such as WM hyperintensities on FLAIR images, were excluded from the two healthy cohorts. R1.4

Assuming a myelin water content of 50%, the MVF of 17.32% in controls, 18.19% in siblings, and 16.02% in patients translate to MWFs of 8.66%, 9.10%, and 8.01%, respectively. These concentrations are in good agreement with previous studies using myelin water imaging[49–51]. The values are also in good agreement with a conversion between MWF and MVF presented recently[52]. Note, however, that myelin not only affects the R_2^* of myelin water but all water in the vicinity of myelin. Even without myelin water, myelin would have an effect on $R_2^*(\theta)$, since it induces non-local field inhomogeneities that reach well beyond the space occupied by myelin water. The range of both iron and myelin content is in agreement with literature values. For iron, Hallgren and Sourander report a standard deviation of 8.8 mg per kg WM tissue in subjects with an age range of 30 to 100 years. While WM iron plateaus after the age of 35[15], myelin is known to decrease with healthy aging[53,54], leading to a range of myelin concentrations in healthy adults of different ages. Vavasour et al. reported a MWF of 8.9 ± 1.0% in NAWM of MS patients, which is in good agreement the MVF of 16.02 ± 2.07% in our patient cohort[40].

By computing $R_2^*(\theta)$, spatial information is lost. In return, the ability to fit an orientation-dependent model to the acquired R_2^* data is gained, providing a unique solution for the average global WM myelin and iron content. Since diffuse damage appears to accompany disease progression in MS[21], quantitative whole WM estimates for iron and/or myelin may be sensitive markers for disease progression. If this is the case, the scan for R_2^* mapping would be readily available on most current MRI scanners. Such approach would be clinically attractive because it provides simple quantitative whole WM estimates for average myelin and iron content. Further correlation with clinical data[55] or biochemical data, such as serum ferritin levels[56] would be straightforward. Note also that 3D gradient echo MRI will likely become part of routine imaging protocols for MS, as it is required for the detection of the central vein sign as a diagnostic marker for MS[57–61]. Lastly, this approach may also be sensitive to diffuse WM-wide remyelination rendered possible by future treatment approaches for MS, and may complement measures of remyelination in focal lesions using magnetization transfer imaging[62], myelin water imaging[28,63,64], or MR phase based approaches[65,66].

This work has some limitations. While the model yields realistic myelin and iron estimates, it should be kept in mind that these values are averages across the entire WM and regional variations of myelin and iron are not captured. For a particular voxel, the tissue composition is not known and variations between different brain areas are to be expected. By pooling voxels from across the entire WM, these regional differences are averaged out and $R_2^*(\theta)$ becomes accessible, allowing for the determination of realistic myelin and iron concentrations with high adjusted R^2, albeit at the loss of spatial information.
However, for fibre tracts that cover a sufficiently large range of orientations, it may be possible to obtain tract-specific concentrations of myelin and iron. Such measurements may be aided by acquisitions at different head orientations, but clinical feasibility of such approach would be limited. Furthermore, since we avoided using an FA threshold for the selection of WM, voxels with low FA and

poorly defined local fibre orientation were included in the analysis and averaged with other voxels. Voxels with crossing fibres pose challenges to the model as well as to the analysis. Crossing fibres may be present in voxels measured across all fibre orientations, and may subsequently be measured as an orientation-independent $R_2^*(\theta)$ contribution. By fitting the numerically obtained $R_2^*(\theta)$ curves to *in vivo* $R_2^*(\theta)$, the model may overestimate iron content and underestimate myelin content due to the presence of crossing fibres. Nevertheless, this is primarily a result of the diffusion acquisition techniques of fibre orientation in *in vivo* data, and not of the efficacy of the numerical model. Advanced diffusion scans, such as diffusion basis spectrum imaging[67] and higher spatial resolution would alleviate some of the issues by reducing the proportion of voxels with crossing fibres. Furthermore, in MS lesions with profound axonal loss, the tissue orientation is also ill-defined. However, there was almost no difference in $R_2^*(\theta)$ when lesions were included or excluded[20]. This finding suggests that the step of lesion exclusion may be omitted for the investigation of non-lesional WM in MS using the proposed approach. Since MS is associated with atrophy of about 0.5% per year[68,69], the question arises on how the proposed approach is affected by tissue loss. Brain atrophy in MS is well studied, and its quantification was suggested to aid clinical assessment of MS[68]. While atrophy may target certain structures more than others, it is agnostic to the angle between fibres and B_0 during an MRI scan. With atrophy, the averaging that leads to the $R_2^*(\theta)$ curve happens across a smaller number of voxels, which reduces the signal-to-noise ratio but does not affect the overall shape of the $R_2^*(\theta)$ curve. Atrophy would have to target a) a certain angle range and b) a certain R_2^* within that angle range in order to distort the $R_2^*(\theta)$ curve. This would be a highly unnatural process.

We provide additional insight on the iron related c_0 coefficient of an empirical model for $R_2^*(\theta)$[11], with a clear correlation displayed between coefficient c_0 and iron concentration. By including an iron-dependent slope of 0.081 ± 0.002 s^{-1} per mg iron per kg tissue, it may become possible to disentangle the contributions of iron from overall $R_2^*(\theta)$, with the remaining constant offset describing other tissue contributions to R_2^*. The obtained slope is in good agreement with the slope of 0.100 ± 0.007 s^{-1} at 0.14 BSA measured in the phantom, and with the slope of 0.100 s^{-1} per mg iron per kg tissue reported for WM in a previous post-mortem study[1].

For the numerical model, several assumptions and simplifications were made:

1. We kept the number of simulated axons fixed and used the g-ratio to control the amount of myelin, in order for myelin content to vary as a continuous variable. With only a few axons within the simulated volume, it is not possible to control myelin content via e.g. myelinated versus non-myelinated axons or the total number of axons. The g-ratios corresponding to the best fits have therefore no direct biological meaning and were converted to myelin content.

2. For ferritin, we assumed that all ferritin molecules are loaded with the same number of 4500 iron atoms. In reality, ferritin is mostly loaded with fewer than 4500 iron atoms[70]. Therefore, the iron content determined with our approach may not be translated to a number of ferritin molecules.

3. Only a small piece of WM was simulated due to high computational cost. The reasons are that ferritin and axons have length scales that differ by three orders of magnitude and that the simulation has to be performed in three dimensions.

4. For similar reasons, we did not include vasculature in the model, which is another two orders of magnitude larger than axons. A considerable proportion of the blood resides in blood vessels that run in parallel with WM tracts[71], causing a tissue orientation effect in gradient echo dynamic susceptibility contrast perfusion MRI[72,73]. Veins should therefore also contribute to R_2^* in an orientation-dependent manner. However, the total blood volume in WM is only about 2.6%[74], resulting in a venous WM blood volume of less than 2%. Moreover, the blood volume in NAWM of patients with MS is only marginally lower relative to controls[75].

5. Diffusion of the proton spins was not taken into account and the signal loss was assumed to be dominated by static dephasing. The diffusion lengths in the experimental data are much larger than the characteristic lengths of the field inhomogeneities produced by both ferritin and axons[26], suggesting that motional narrowing may have an impact on R_2^*. With static dephasing, the model fit to an individual subject takes about half a day on a typical personal computer (Intel i7, 32 GB of memory). The modelling of diffusion effects would increase the computational cost by at least two orders of magnitude, making the fitting of a total of 91 subjects computationally infeasible. Even without modelling diffusion-mediated effects, we can see that iron-induced contributions are required to fit to experimental R_2^* measured in WM. Furthermore, the iron-dependent slope derived from the phantom

experiment (0.100 ± 0.007 s^{-1} per mg iron per kg) is in close agreement to the slope derived from the static simulation (0.081 ± 0.002 s^{-1} per mg iron per kg). This implies that regardless of a static model or a model with diffusion, the contributions of iron on overall R_2^* are additive, and independent of whether diffusion is modelled.

6. By fitting a mono-exponential decay to the multi echo data, we neglected the multi-exponential nature of R_2^* relaxation, which cannot be captured with a scan that only has 5 echoes.

7. We kept the T_2 of myelin water, intracellular and extracellular water constant between the three cohorts. This simplification seems justified in a regime that is dominated by static dephasing.

In conclusion, we presented an approach for estimating average global non-lesional myelin and iron content from orientation-dependent R_2^* data. Application of the proposed numerical tissue model to *in vivo* data shows significant loss of iron and myelin in subjects with MS, in line with histopathological reports, and a significant increase in iron in healthy siblings of subjects with MS. The proposed approach may be useful for the assessment of disease progression in MS.

Funding

This study was funded by NSERC (016-05371) and the National MS Society (RG-1507-05031). D. Kor and J. Doucette were funded by NSERC USRA (USRA 513103-2017, USRA 527378-2018, and USRA 497681-2016). C. Birkl was funded by the Austrian Science Fund (J4038-B27). V. Wiggermann was supported by a graduate studentship award from the MS Society of Canada (EGID 2002). A. Rauscher is funded by Canada Research Chairs.

References

1. Langkammer C, Krebs N, Goessler W, et al. Quantitative MR imaging of brain iron: a postmortem validation study. *Radiology*. 2010;257(2):455-462.

2. Walsh AJ, Blevins G, Lebel RM, Seres P, Emery DJ, Wilman AH. Longitudinal MR Imaging of Iron in Multiple Sclerosis: An Imaging Marker of Disease. *Radiology*. August 2013.

3. Walsh AJ, Lebel RM, Eissa A, et al. Multiple sclerosis: validation of MR imaging for quantification and detection of iron. *Radiology*. 2013;267(2):531-542.

4. Khalil M, Langkammer C, Pichler A, et al. Dynamics of brain iron levels in multiple sclerosis: A longitudinal 3T MRI study. *Neurology*. 2015;84(24):2396-2402.

5. Khalil M, Langkammer C, Ropele S, et al. Determinants of brain iron in multiple sclerosis: a quantitative 3T MRI study. *Neurology*. 2011;77(18):1691-1697.

6. Schweser F, Raffaini Duarte Martins AL, Hagemeier J, et al. Mapping of thalamic magnetic susceptibility in multiple sclerosis indicates decreasing iron with disease duration: A proposed mechanistic relationship between inflammation and oligodendrocyte vitality. *NeuroImage*. 2018;167:438-452.

7. Hernández-Torres E, Wiggermann V, Machan L, et al. Increased mean R2* in the deep gray matter of multiple sclerosis patients: Have we been measuring atrophy? *J Magn Reson Imaging*. 0(0).

8. Bender B, Klose U. The in vivo influence of white matter fiber orientation towards B(0) on T2* in the human brain. *NMR Biomed*. 2010;23(9):1071-1076.

9. Denk C, Hernandez Torres E, MacKay A, Rauscher A. The influence of white matter fibre orientation on MR signal phase and decay. *NMR Biomed*. 2011;24(3):246-252.

10. Lee J, van Gelderen P, Kuo L-W, Merkle H, Silva AC, Duyn JH. T2*-based fiber orientation mapping. *NeuroImage*. 2011;57(1):225-234.

11. Lee J, Shin H-G, Jung W, Nam Y, Oh S-H, Lee J. An R2* model of white matter for fiber orientation and myelin concentration. *NeuroImage*. 2017;162:269-275.

12. Oh S-H, Kim Y-B, Cho Z-H, Lee J. Origin of B0 orientation dependent R2(*) (=1/T2(*)) in white matter. *NeuroImage*. 2013;73:71-79.

13. Xu T, Foxley S, Kleinnijenhuis M, Chen WC, Miller KL. The effect of realistic geometries on the susceptibility-weighted MR signal in white matter. *Magn Reson Med*. 2018;79(1):489-500.

14. Wharton S, Bowtell R. Fiber orientation-dependent white matter contrast in gradient echo MRI. *Proc Natl Acad Sci U S A*. 2012;109(45):18559-18564.

15. HALLGREN B, SOURANDER P. The effect of age on the non-haemin iron in the human brain. *J Neurochem*. 1958;3(1):41-51.

16. Krebs N, Langkammer C, Goessler W, et al. Assessment of trace elements in human brain using inductively coupled plasma mass spectrometry. *J Trace Elem Med Biol Organ Soc Miner Trace Elem GMS*. 2014;28(1):1-7.

17. Filippi M, Bozzali M, Rovaris M, et al. Evidence for widespread axonal damage at the earliest clinical stage of multiple sclerosis. *Brain J Neurol*. 2003;126(Pt 2):433-437.

18. Tortorella C, Viti B, Bozzali M, et al. A magnetization transfer histogram study of normal-appearing brain tissue in MS. *Neurology*. 2000;54(1):186-193.

19. Laule C, Vavasour IM, Moore GRW, et al. Water content and myelin water fraction in multiple sclerosis. A T2 relaxation study. *J Neurol*. 2004;251(3):284-293.

20. Hernández-Torres E, Wiggermann V, Hametner S, et al. Orientation Dependent MR Signal Decay Differentiates between People with MS, Their Asymptomatic Siblings and Unrelated Healthy Controls. *PLoS ONE*. 2015;10(10):e0140956.

21. Kutzelnigg A, Lucchinetti CF, Stadelmann C, et al. Cortical demyelination and diffuse white matter injury in multiple sclerosis. *Brain*. 2005;128(11):2705-2712.

22. Haider L, Zrzavy T, Hametner S, et al. The topograpy of demyelination and neurodegeneration in the multiple sclerosis brain. *Brain J Neurol*. 2016;139(Pt 3):807-815.

23. Hametner S, Wimmer I, Haider L, Pfeifenbring S, Bruck W, Lassmann H. Iron and neurodegeneration in the multiple sclerosis brain. *Ann Neurol*. 2013;74(6):848-861.

24. Birkl C, Langkammer C, Krenn H, et al. Iron mapping using the temperature dependency of the magnetic susceptibility. *Magn Reson Med*. 2015;73(3):1282-1288.

25. Deistung A, Schweser F, Reichenbach JR. Overview of quantitative susceptibility mapping. *NMR Biomed*. July 2016.

26. Duyn JH, Schenck J. Contributions to magnetic susceptibility of brain tissue. *NMR Biomed*. 2017;30(4).

27. Liu C. Susceptibility tensor imaging. *Magn Reson Med Off J Soc Magn Reson Med Soc Magn Reson Med*. 2010;63(6):1471-1477.

28. Mackay A, Whittall K, Adler J, Li D, Paty D, Graeb D. <I>In vivo</I> visualization of myelin water in brain by magnetic resonance. *Magn Reson Med*. 1994;31(6):673-677.

29. Harrison PM, Arosio P. The ferritins: molecular properties, iron storage function and cellular regulation. *Biochim Biophys Acta BBA - Bioenerg*. 1996;1275(3):161-203.

30. Trapp BD, Kidd GJ. Chapter 1 - Structure of the Myelinated Axon. In: *Myelin Biology and Disorders*. San Diego: Academic Press; 2004:3-27.

31. Schenck JF. Magnetic resonance imaging of brain iron. *J Neurol Sci*. 2003;207(1-2):99-102.

32. Jenkinson M, Beckmann CF, Behrens TEJ, Woolrich MW, Smith SM. FSL. *NeuroImage*. 2012;62(2):782-790.

33. Misaki M, Savitz J, Zotev V, et al. Contrast enhancement by combining T1- and T2-weighted structural brain MR Images. *Magn Reson Med*. 2015;74(6):1609-1620.

34. Roosendaal SD, Geurts JJG, Vrenken H, et al. Regional DTI differences in multiple sclerosis patients. *NeuroImage*. 2009;44(4):1397-1403.

35. Kim S-H, Kwak K, Hyun J-W, et al. Diffusion tensor imaging of normal-appearing white matter in patients with neuromyelitis optica spectrum disorder and multiple sclerosis. *Eur J Neurol*. 2017;24(7):966-973.

36. Öner M, Kocakoç İD. JMASM 49: A Compilation of Some Popular Goodness of Fit Tests for Normal Distribution: Their Algorithms and MATLAB Codes (MATLAB). *J Mod Appl Stat Methods*. 2017;16(2).

37. Soellinger M, Langkammer C, Seifert-Held T, Fazekas F, Ropele S. Fast bound pool fraction mapping using stimulated echoes. *Magn Reson Med*. 2011;66(3):717-724.

38. Todorich B, Pasquini JM, Garcia CI, Paez PM, Connor JR. Oligodendrocytes and myelination: The role of iron. *Glia*. October 2008.

39. Bagnato F, Hametner S, Boyd E, et al. Untangling the R2* contrast in multiple sclerosis: A combined MRI-histology study at 7.0 Tesla. *PloS One*. 2018;13(3):e0193839.

40. Vavasour IM, Huijskens SC, Li DK, et al. Global loss of myelin water over 5 years in multiple sclerosis normal-appearing white matter. *Mult Scler Houndmills Basingstoke Engl*. August 2017:1352458517723717.

41. Laule C, Pavlova V, Leung E, et al. Diffusely abnormal white matter in multiple sclerosis: further histologic studies provide evidence for a primary lipid abnormality with neurodegeneration. *J Neuropathol Exp Neurol*. 2013;72(1):42-52.

42. Wiggermann V, Hametner S, Hernández-Torres E, et al. Susceptibility-sensitive MRI of multiple sclerosis lesions and the impact of normal-appearing white matter changes. *NMR Biomed*. 2017;30(8):e3727.

43. Chao MJ, Barnardo MCNM, Lincoln MR, et al. HLA class I alleles tag HLA-DRB1*1501 haplotypes for differential risk in multiple sclerosis susceptibility. *Proc Natl Acad Sci U S A*. 2008;105(35):13069-13074.

44. Haider L, Fischer MT, Frischer JM, et al. Oxidative damage in multiple sclerosis lesions. *Brain*. 2011;134(7):1914-1924.

45. Lassmann H, van Horssen J. Oxidative stress and its impact on neurons and glia in multiple sclerosis lesions. *Biochim Biophys Acta*. 2016;1862(3):506-510.

46. Levine SM. The Role of Iron in the Pathogenesis of Experimental Allergic Encephalomyelitis and Multiple Sclerosis. *N Y Acad Sci Ann*. 2004;1012:252-266.

47. Xia Z, Steele SU, Bakshi A, et al. Assessment of Early Evidence of Multiple Sclerosis in a Prospective Study of Asymptomatic High-Risk Family Members. *JAMA Neurol*. 2017;74(3):293-300.

48. Gabelic T, Ramasamy DP, Weinstock-Guttman B, et al. Prevalence of radiologically isolated syndrome and white matter signal abnormalities in healthy relatives of patients with multiple sclerosis. *AJNR Am J Neuroradiol*. 2014;35(1):106-112.

49. Groeschel S, Hagberg GE, Schultz T, et al. Assessing White Matter Microstructure in Brain Regions with Different Myelin Architecture Using MRI. *PLOS ONE*. 2016;11(11):e0167274.

50. Meyers SM, Kolind SH, MacKay AL. Simultaneous measurement of total water content and myelin water fraction in brain at 3T using a T2 relaxation based method. *Magn Reson Imaging*. 2017;37:187-194.

51. Meyers SM, Laule C, Vavasour IM, et al. Reproducibility of myelin water fraction analysis: a comparison of region of interest and voxel-based analysis methods. *Magn Reson Imaging*. April 2009.

52. Jung W, Lee J, Shin H-G, et al. Whole brain g-ratio mapping using myelin water imaging (MWI) and neurite orientation dispersion and density imaging (NODDI). *NeuroImage*. September 2017.

53. Peters A. The effects of normal aging on myelin and nerve fibers: A review. *J Neurocytol*. 2002;31(8):581-593.

54. Wiggins RC, Gorman A, Rolsten C, Samorajski T, Ballinger WE, Freund G. Effects of aging and alcohol on the biochemical composition of histologically normal human brain. *Metab Brain Dis*. 1988;3(1):67-80.

55. Cohen RA, Kessler HR, Fischer M. The Extended Disability Status Scale (EDSS) as a predictor of impairments of functional activities of daily living in multiple sclerosis. *J Neurol Sci*. 1993;115(2):132-135.

56. Sfagos C, Makis AC, Chaidos A, et al. Serum ferritin, transferrin and soluble transferrin receptor levels in multiple sclerosis patients. *Mult Scler Houndmills Basingstoke Engl*. 2005;11(3):272-275.

57. Sati P, Oh J, Constable RT, et al. The central vein sign and its clinical evaluation for the diagnosis of multiple sclerosis: a consensus statement from the North American Imaging in Multiple Sclerosis Cooperative. *Nat Rev Neurol*. 2016;12(12):714-722.

58. Maggi P, Absinta M, Grammatico M, et al. Central vein sign differentiates Multiple Sclerosis from central nervous system inflammatory vasculopathies. *Ann Neurol*. 2018;83(2):283-294.

59. Mistry N, Abdel-Fahim R, Samaraweera A, et al. Imaging central veins in brain lesions with 3-T T2*-weighted magnetic resonance imaging differentiates multiple sclerosis from microangiopathic brain lesions. *Mult Scler J*. 2016;22(10):1289-1296.

60. Samaraweera APR, Clarke MA, Whitehead A, et al. The Central Vein Sign in Multiple Sclerosis Lesions Is Present Irrespective of the T2* Sequence at 3 T. *J Neuroimaging*. 2017;27(1):114-121.

61. Samaraweera APR, Falah Y, Pitiot A, Dineen RA, Morgan PS, Evangelou N. The MRI central vein marker; differentiating PPMS from RRMS and ischemic SVD. *Neurol Neuroimmunol Neuroinflammation*. 2018;5(6):e496.

62. Ropele S, Fazekas F. Magnetization Transfer MR Imaging in Multiple Sclerosis. *Neuroimaging Clin N Am*. 2009;19(1):27-36.

63. Laule C, Kozlowski P, Leung E, Li DKB, MacKay AL, Moore GRW. Myelin water imaging of multiple sclerosis at 7 T: correlations with histopathology. *NeuroImage*. 2008;40(4):1575-80.

64. Prasloski T, Rauscher A, MacKay AL, et al. Rapid whole cerebrum myelin water imaging using a 3D GRASE sequence. *NeuroImage*. 2012;63(1):533-539.

65. Wiggermann V, Hametner S, Hernández-Torres E, et al. Cover Image, Volume 30, Issue 8. *NMR Biomed*. 2017;30(8):i-i.

66. Wiggermann V, Hernández Torres E, Vavasour IM, et al. Magnetic resonance frequency shifts during acute MS lesion formation. *Neurology*. 2013;81(3):211-218.

67. Wang Y, Wang Q, Haldar JP, et al. Quantification of increased cellularity during inflammatory demyelination. *Brain J Neurol*. 2011;134(Pt 12):3590-3601.

68. Rocca MA, Battaglini M, Benedict RHB, et al. Brain MRI atrophy quantification in MS: From methods to clinical application. *Neurology*. 2017;88(4):403-413.

69. Zivadinov R, Jakimovski D, Gandhi S, et al. Clinical relevance of brain atrophy assessment in multiple sclerosis. Implications for its use in a clinical routine. *Expert Rev Neurother*. 2016;16(7):777-793.

70. Brooks RA, Vymazal J, Goldfarb RB, Bulte JW, Aisen P. Relaxometry and magnetometry of ferritin. *Magn Reson Med*. 1998;40(2):227-235.

71. Okudera T, Huang YP, Fukusumi A, Nakamura Y, Hatazawa J, Uemura K. Micro-angiographical studies of the medullary venous system of the cerebral hemisphere. *Neuropathol Off J Jpn Soc Neuropathol*. 1999;19(1):93-111.

72. Hernández-Torres E, Kassner N, Forkert ND, et al. Anisotropic cerebral vascular architecture causes orientation dependency in cerebral blood flow and volume measured with dynamic susceptibility contrast magnetic resonance imaging. *J Cereb Blood Flow Metab Off J Int Soc Cereb Blood Flow Metab*. June 2016.

73. Doucette J, Wei L, Hernández-Torres E, et al. Rapid solution of the Bloch-Torrey equation in anisotropic tissue: Application to dynamic susceptibility contrast MRI of cerebral white matter. *NeuroImage*. 2018;185:198-207.

74. Leenders KL, Perani D, Lammertsma AA, et al. Cerebral blood flow, blood volume and oxygen utilization. Normal values and effect of age. *Brain J Neurol*. 1990;113 (Pt 1):27-47.

75. Lapointe E, Li DKB, Traboulsee AL, Rauscher A. What Have We Learned from Perfusion MRI in Multiple Sclerosis? *AJNR Am J Neuroradiol*. January 2018.

Figure Captions

Figure 1: An example of the magnetic field inhomogeneities generated by myelinated axons and ferritin computed using equation 5. For this example, the tissue model was oriented at an angle of 90° relative to the main magnetic field.

Figure 2: Simulated $R_2^*(\theta)$ curves for different iron and myelin volume fractions. The red curve with markers corresponds to typical R_2^* measured in volunteers at 3T. Due to the orientation dependency of myelin related R_2^*, this curve cannot be obtained with myelin alone (green dashed, yellow dashed, purple solid line). Without iron, the orientation dependency may be qualitatively the same as in the measured data, but the overall R_2^* is too low (yellow and green dashed lines). On the other hand, with a myelin content that results in the correct R_2^* at low angles, the orientation dependency (ΔR_2^*) is too large (purple solid). $R_2^*(\theta)$ curves with different combinations of iron and myelin content have been simulated (green, blue and orange solid). Relative to the optimal simulated R_2^* curve (red solid with markers), these curves have the same R_2^* at low angles. At higher angles, however, the curves deviate significantly from the realistic simulated R_2^* curve, due to the high myelin contents needed to achieve realistic $R_2^*(0^\circ)$ values.

Figure 3: (A) All simulated curves (solid lines) with fitted parameters overlaid on experimental R_2^* data (points) with patients with MS in green, healthy siblings of patients with MS in blue and unrelated healthy controls in red. (B, C and D): The simulated curves from the individual cohorts of healthy controls, siblings of MS patients, and MS patients, respectively.

Figure 4: Iron concentration and myelin volume fraction (MVF) values for all three groups computed by fitting the numerical model. Coloured dots represent the fitted parameters for individual curves grouped in either MS patients (green), healthy siblings of MS patients (blue) and unrelated healthy controls (red). Significant differences in iron concentration were observed with comparisons between healthy siblings of MS patients and unrelated healthy controls ($p = 0.039$), between unrelated healthy

controls and MS patients ($p = 0.0016$), and between healthy siblings of MS patients and MS patients ($p < 0.0001$). For MVF values, significant differences were observed with the comparison between healthy siblings of MS patients and MS patients ($p = 0.0019$). However, the comparison between unrelated healthy controls and healthy siblings of MS patients yielded no significant difference in MVF ($p = 0.17$), and remained insignificant even without the Bonferroni-Holm correction. Although no significant difference in MVF ($p = 0.072$) was observed the comparison between unrelated healthy controls and MS patients, it should be noted that all reported p-values are corrected for Type I error via the Bonferroni-Holm method. Pairwise comparison between MS patients and unrelated healthy controls yielded an uncorrected $p = 0.036$.

Figure 5: R_2^* measured in a phantom of 24 different concentrations of BSA and ferritin (iron). R_2^* values increase with increasing concentrations of BSA and ferritin. For a single value of measured R_2^*, several combinations of BSA and iron concentration are possible.

Tables

	MS Patients	Siblings of MS patients	Healthy Controls
N (female/male)	39 (35/4)	31 (20/11)	30 (25/5)
Age (years)	[32 – 69] (49.7 ± 10.1)	[30 – 67] (50.6 ± 11.0)	[30 – 67] (50.6 ± 11.3)
Age at disease onset (years)	[17 – 56] (32.4 ± 8.0)	N/A	N/A
Disease Duration (DD, years)	[3 – 41] (17.2 ± 9.3)	N/A	N/A
Expanded disability status scale	[0 – 6.5] median 2.5	N/A	N/A

Table 1: The demographic of subjects across all three cohorts.

	Iron Concentration [range] (mean ± STD) [mg/kg]	Myelin Volume Fraction [range] (mean ± STD) [%]	Adjusted R^2 [range] (mean ± STD)
Controls	[27.9 - 57.2] (43.1 ± 8.3)	[12.92 - 22.84] (17.32 ± 2.20)	[0.84 - 0.99] (0.94 ± 0.04)
Siblings	[31.4 - 61.0] (47.8 ± 8.2)	[14.50 - 25.23] (18.19 ± 2.98)	[0.70 - 0.99] (0.93 ± 0.07)
Patients	[15.7 - 50.7] (35.6 ± 8.9)	[12.12 - 20.11] (16.02 ± 2.07)	[0.76 - 0.99] (0.93 ± 0.05)

Table 2: The distribution of fitted parameters for all three groups with their corresponding coefficients of determination. Relative to unrelated healthy controls, significantly increased mean iron concentration was found in healthy siblings of MS patients. Significantly decreased mean iron concentration was found in MS patients compared to the other two groups. Relative to healthy siblings of MS patients, significantly decreased myelin volume fraction was found in MS patients.